A Survey on Static Modeling of Miniaturized Pneumatic Artificial Muscles with New Model and Experimental Results

K. P. Ashwin [*], and A. Ghosal [†]

Abstract

Pneumatic Artificial Muscles (PAM) are linear pneumatic actuators consisting of a flexible bladder with a set of in-extensible fibers woven as a sheath on the outside. Upon application of pressure, the actuators contract or expand based on the angle of winding of the braid. Due to the similarity in properties of the actuators with biological muscles and the advantages thereof, these are increasingly being used in many robotic systems and mechanisms. This necessitates the development of mathematical models describing their mechanics for optimal design as well as for application in control systems. This paper presents a survey on different mathematical models described in the literature for representing the statics of PAM. Since it is observed that the validity of existing static models, based on energy balance methods, are not consistent with changes in parameters when applied to their miniaturized versions (MPAM), a new model has been proposed. The model takes into account material properties of the bladder as well as the end-effects which are prominent for MPAMs. Experiments conducted on fabricated MPAMs, of different diameters and lengths, show that the proposed model predicts the pressure-deformation characteristics of MPAMs with maximum error of less than 7% error.

Keywords: McKibben actuators, Miniaturized pneumatic artificial muscles, Modeling, Experimental validation.

1 Introduction

In 1958, Richard H. Gaylord patented a 'Fluid Actuated Stroking Device' which is 'an expansible chamber device comprising a bladder confined within a braided sheath...adapted to be energized by a fluid' [1]. The bladder which is sealed on one end is made of flexible material and the braided sheath is usually woven using in-extensible fibers. The device is essentially a linear actuator with the interesting property that if the angle at which the outer sheath is braided differs from a particular locking angle, it contracts or expands upon pressurization of the fluid contained in the bladder. This invention gained popular attention when later used by McKibben in a design of orthotic wheelchair [2]. Due to the similarity of this flexible actuator with biological muscles, the device is often identified by the name 'McKibben Muscles' or 'Fluidic Artificial Muscles (FAMs)'. For several years, these actuators did not achieve much commercial success probably due to the bulky accessories which are required to energize the system or due to the faster progress in the development of electric motors and other actuators. More recently since the 1980s, the actuator have regained its commercial and academic attention due to its unique advantages. The FAMs which make use of pressurized air are also called 'Pneumatic Artificial Muscles (PAMs)' and are now extensively studied by engineers especially in the field of bio-inspired [3] and medical robotics [4]. In [5], the authors have listed in detail, the major developments towards the evolution of Pneumatic Artificial Muscles.

Among the different types of conventional actuating mechanisms such as electric motors, pneumatic pistons, shape memory alloys etc. as well as the flexible actuators used in robots [6], artificial muscles stand out due to their following advantages:

[*]Graduate Student at the Robotics and Design Lab, Department of Mechanical Engineering, Indian Institute of Science, Bangalore 560012, India, email: ashwinkp@iisc.ac.in

[†]Corresponding Author, Professor, Department of Mechanical Engineering, Indian Institute of Science, Bangalore, email: asitava@iisc.ac.in.

- High power to weight ratio: The earliest commercial PAM called 'Rubbertuator' by Bridgestone corporation and Hitachi weighed about 6 kg and could lift a mass of approximately 2 kg (refer [7], [8]). At present, the PAMs manufactured by companies like Festo [4] has a lifting force of 6000 N while weighing only about 800 grams.

- Flexibility and compliance: An unpressurized PAM exhibits the same flexibility as that of the bladder but it becomes stiff while remaining reasonably compliant upon pressurization. This compliance is a necessity for the development of medical devices such as minimal invasive surgical tools ([9], [10], [11]) and rehabilitation robots (refer [7], [12], [13]).

- Compatibility with human environment: The primary actuation mechanism of PAM is pressurized air or pressurized inert gas. Hence, it is safer compared to other devices which use electricity, heat or chemically active substances. The only practical safety concern regarding PAM could be the rupture of inner bladder under high pressure. However, by controlling volume flow rate of air into PAMs, this issue can be addressed.

- Low cost in fabrication: A simple PAM could be fabricated from inexpensive off-the-shelf materials. Hence the manufacturing cost of PAMs is very low compared to other actuators in the same functionality regime. However, it may be noted that PAMs require pneumatic circuitry which increases the initial cost.

Due to the above mentioned advantages, PAMs have found many applications in the robotic industry. A detailed survey on robots which make use of PAMs spanning the domains such as biologically inspired robots, rehabilitation devices, industrial robots, exoskeletons and aerospace applications can be found in [14]. The application of PAM in haptic force sensing for laparoscopic surgery [15] and as a 'dummy device' in pedestrian safety systems [16] suggest the scope of indirect application of PAMs in engineering. Particularly interesting are the miniaturized versions of PAMs, also called MPAMs, where the diameter is less than 5 mm. Due to the small size, these actuators are used in different applications such as wearable hand exoskeletons [17], cardiac compression devices [18], tool manipulation in surgical devices ([19], [20], [10]) etc. Miniaturized PAMs of diameter less than 2 mm can be bundled into an organized muscle structure for lifting heavy loads. An advantage of using multiple PAMs as bundle or in parallel is the ability to recruit selected muscles as per the load requirement. The variable recruitment technique of muscle bundles is more energy efficient compared to a single muscle of equivalent capacity and are studied in references [21], [22], [23], [24] and [25]. It is shown in [26] that bundling MPAMs exhibit better contraction ratio compared to a single muscle of same diameter. By adjusting the braiding characteristics of PAM or by clubbing two PAMs with different characteristics, the PAM could generate a moment resulting in bending actuators [27], [28] and [29]. From these references, we can see that researchers across the world are putting considerable emphasis in this promising field.

With the widespread use of PAMs and MPAMs in robotics, accurate mathematical description of underlying mechanics has become a necessity. However, due to the complex interaction of forces in a PAM, this task is not trivial. Nonetheless, many attempts have been made in this regard due to two reasons. Firstly, a mathematical model would help to improve the control system of robots, especially in implementing model based control systems [30], [31], [15]. In such cases however, it is desired to have an easily implementable and computationally efficient model to improve the response of the controller. Secondly, a model with sufficient parameters helps to efficiently choose or fabricate an actuator with optimized qualities intended for a particular task. In this case, an accurate model which describes the mechanics of PAM based on actuator dimensions, braiding characteristics, material properties etc. is preferred. Like any other pneumatic systems, PAM exhibits hysteresis which is a major hindrance in modeling statics and dynamics of PAM. Due to static frictional forces and nonlinearity in the material of the bladder, a quasi-static contraction (or elongation) of PAM shows different curves for force vs length and pressure vs length plots for compression as well as decompression of air. In force modeling methods, this additional frictional force is generally added (or subtracted) from a mean curve for contraction (and elongation) of PAM. This frictional force, as may be seen in the later sections of this article, are mostly empirically calculated. For modelling the dynamics of

PAM, the rate of change of state of PAM is related to the change in input parameters where kinetic friction is also included in the model.

In the review paper by Tondu [32], the author meticulously reviewed the major static and dynamic modeling improvements carried out by well-known researchers in the field. Starting from the simple and arguably the first static model proposed by Schulte [33], the author carefully addressed different physical considerations which could improve the basic model such as the inclusion of material properties, non-cylindrical end-effects, representation of PAM as a fiber-reinforced membrane model as well as muscle hysteresis. The author lists the necessary considerations, reasonable assumptions as well as precautions to be taken in deriving the static and dynamic formulae representing the actuation of PAM. However, since the objective of the paper is to identify accurate means to describe the physics of PAM, a few models in the literature which rely on empirical formulations as well as the models which provide only minor improvements from the standard equations are not detailed in Tondu's article. In this paper, we update the review paper by Tondu in two ways: firstly, in our review we include some modeling considerations that are not mentioned in Tondu's paper in section 2. Secondly, it has been noted in literature as well as from the experiments conducted by the authors that static characteristics of MPAMs are not always consistent with the models used for normal sized PAMs due to the larger ratio between the volume occupied by bladder and the internal volume of the bladder and the end effects. Hence, most models used in describing MPAM statics necessitates correction factors to be included in models for larger PAMs. In order to address this gap in the literature, this paper also presents a new approach in modeling statics of MPAM. A detailed model and its comparison to existing models is presented in section 3. In section 4, we present the details of the experiments done to validate the model. We present experimental results for MPAMs with two different diameters and of three different lengths each. It is shown that the computed results obtained from the proposed model lie within the rage of experimental results and the maximum error is less than 7%. Finally, conclusions of this work are presented in section 5.

2 Review of static modeling of PAMs

In this section, we introduce models used by different research teams to describe the statics of PAM. Many models which assume quasi-static motion do not consider hysteresis into account since accurate phenomenological description of hysteresis is not yet available and many control system strategies use the mean value between contraction and extension profiles [30], [34], [16]. As described before, in case of force balance formulations, these hysteresis forces can be added (or subtracted) in case the hysteresis effect is non-negligible. Also, extensile PAMs are not commonly used compared to the contractile PAMs since additional arrangements are required to avoid the buckling effect. In [35] the authors compare the performance differences between contractile and extensile muscles. It is shown that the derived mathematical models are valid for extensile muscles as well. Hence, most models stated here will assume the primary actuation mode of PAMs as contractile. Finally a few fundamental models mentioned in Tondu's paper are also discussed here for completeness.

We will use the following nomenclature in this paper, unless stated otherwise (refer figure 1):

l_0, r_0 and t_0 represent the length, outer radius and thickness of the bladder before deformation, respectively. After deformation, these quantities change to l, r and t. The quantity $r_i = r_0 - t_0$ represents the initial inner radius of the bladder. Initial and final winding angle of braid are denoted as θ_0 and θ, respectively. The symbol N, m and b represent the number of turns of the braid along the length, number of strands of braid as well as the length of a single braid strand, respectively. The symbol P_i represents the input pressure, $\epsilon = \dfrac{l_0 - l}{l_0}$ represents the strain in the bladder along the axial direction and letters F and κ will be used to represent force and constants in general.

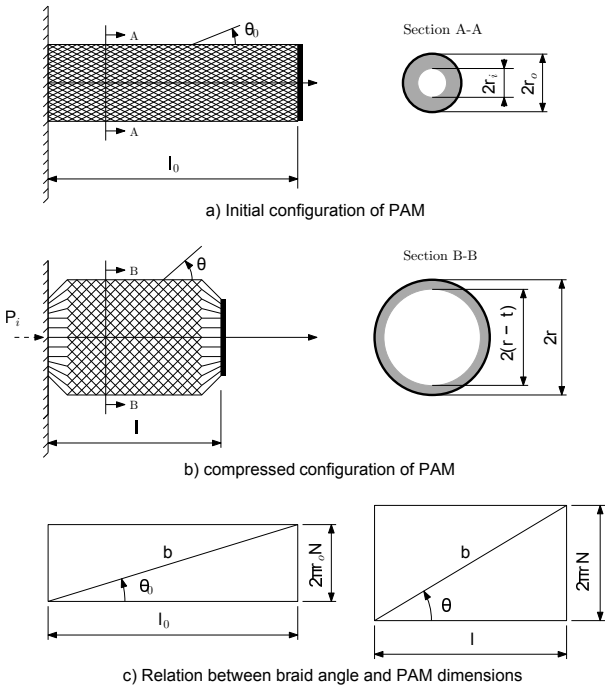

Figure 1: MPAM nomenclature

If we assume that the PAM remains cylindrical after deformation i.e., if the tapering effects at the ends are not considered, we can write the following equations [36]

$$l_0 = b\cos\theta_0, \quad 2\pi r_0 N = b\sin\theta_0 \tag{1}$$

$$l = b\cos\theta, \quad 2\pi r N = b\sin\theta \tag{2}$$

In the above equations, it is assumed that the braid is in contact with the outer surface of the tube at all times and the thickness of the braid is neglected. It is also assumed that the braid material is inextensible.

2.1 Basic modeling strategies

The earliest mathematical model which takes into account the mechanics of a PAM can be found in Gaylord's patent [1]. For static equilibrium of the compressed muscle, the energy provided by the applied pressure ($P_i\ dV$) must be balanced by the work done by the PAM which is carrying the load applied at the tip to a particular distance ($F\ dz$). By expressing the change in volume enclosed by the braided sheath dV and the displacement of the PAM tip dz in terms of the angle of winding, the energy balance formula yield the following expression for force:

$$F^{(1)}_{\text{Gaylord}} = \frac{b^2}{4\pi N^2} P_i \left(3\cos^2\theta - 1\right) \tag{3}$$

In the above equation, the initial cylindrical shape of the bladder is assumed to stay cylindrical even after deformation and the simple kinematic equations of the braid given by equations (1) and (2) are used. The above relation gives the value of final braid angle θ for the applied pressure and axial loading from which we can find the final length of PAM using equation (2). The limiting value of braid angle (and hence, the length) for which the force exerted is maximum can be found by differentiating the above equation with respect to θ and setting to zero. The value $\theta_{\text{limit}} = 54.7°(\ 54°44')$ hence becomes a locking angle for deformation of

PAM, and a PAM wound with a braid at any initial winding angle will theoretically approach this locking angle with an increase in pressure. This model is also found in the literature in its alternate form,

$$F^{(2)}_{\text{Gaylord}} = \pi r_0^2 P_i \left[q_1 \left(1-\epsilon\right)^2 - q_2 \right] \tag{4}$$
$$q_1 = \frac{3}{\tan^2\theta_0}, \quad q_2 = \frac{1}{\sin^2\theta_0}$$

which shows the primary behavior of PAM as a non-linear spring. In this simplistic and first approximation of PAM statics, the volume occupied by air inside the bladder is assumed to be the same as the volume enclosed by the braided sheath. However, this assumption is an over-estimation of pressure energy since the the volume of air inside the bladder is only the volume enclosed by the cylinder formed by its inner radius. In [36], Chou gives an expression for the force taking into account the thickness of bladder:

$$\begin{aligned} F^{(1)}_{\text{Chou}} =& \frac{b^2}{4\pi N^2} P_i \left(3\cos^2\theta - 1\right) + \\ & \pi P_i \left[\frac{bt_0}{N\pi} \left(2\sin\theta - \frac{1}{\sin\theta} \right) - t_0^2 \right] \end{aligned} \tag{5}$$

The experimental comparisons shown in Chou's paper suggest that even though the model is derived based on simplified assumptions, this is a good first approximation. In the coming years, researchers improvised on this basic model by adding correction factors, relaxing the modeling assumptions or adding force terms arising from other physical phenomena contributing to the statics of a PAM.

2.2 Correction factors for Gaylord's model

Gaylord's model assumes the initial cylindrical shape of the PAM to remain cylindrical even after deformation. However, since one end of the PAM is connected to the pressure inlet system and the free end is always sealed, the radial expansion of bladder will be non-uniform. In the clamped ends, the radius of bladder will be the initial radius after deformation. Hence, on either ends of a PAM, the cylinder takes approximately, the shape of a conical frustum. In [37], Tondu modified the basic equation by Gaylord to include a factor 'k_ϵ' which was intended to account for this non cylindrical tip effects. The force was given as

$$F = \pi r_0^2 P_i \left[q_1 \left(1 - k_\epsilon \epsilon\right)^2 - q_2 \right] \tag{6}$$

In their work, to match the experimental results, the factor k_ϵ is chosen as $k_\epsilon = \kappa_1 e^{-P_i} + \kappa_2$, where the constants κ_1 and κ_2 are experimentally calculated. In another work by Itto et al. [38], the value of k_ϵ is chosen as $k_\epsilon = \kappa_1 e^{\kappa_2 P_i} + \kappa_3$ to add more flexibility. In Tondu's model, static frictional force is also included to improve the static characteristics:

$$F_{\text{fstat}} = \mu_s P_i \left(\frac{S^{(1)}_{\text{contact}}}{S^{(1)}_{\text{scale}}} \right) \tag{7}$$

where $S^{(1)}_{\text{contact}} = 2\pi r_0 l_0 \dfrac{\sin\theta_0}{(1-k_\epsilon\epsilon)\sqrt{1-\cos^2\theta_0(1-k_\epsilon\epsilon)^2}}$ is the contact surface between the strands of the braid, μ_s is the coefficient of friction between the braid strands and $S^{(1)}_{\text{scale}}$ is a correction factor for the surface area of contact $S^{(1)}_{\text{contact}}$, since the formulation of the contact surface area assumes flat strands of braid. Taking into account these considerations, the force is given as

$$F_{\text{Tondu}} = \pi r_0^2 P_i \left[q_1 \left(1 - k_\epsilon \epsilon\right)^2 - q_2 \right] \pm \mu_s P_i \left[\frac{S^{(1)}_{\text{contact}}}{S^{(1)}_{\text{scale}}} \right] \tag{8}$$

where the quantity $S^{(1)}_{\text{scale}}$ is experimentally determined. This model is applied in many works such as in the control system design of a multi joint arm in [34] as well as in variable recruitment of PAM bundles in [22] and [25].

An improvement in Tondu's model was proposed by Davis and Caldwell [39], by including a more detailed derivation for the surface area of contact between the braid strands. For a PAM of given dimensions and braiding pattern, the surface area is defined in terms of the minimum angle of winding possible in the stretched state ($\theta_{\min}$):

$$S^{(2)}_{\text{contact}} = \frac{b^2 \sin\theta_{\min} \cos\theta_{\min}}{N \sin\theta \cos\theta} \tag{9}$$

where

$$\theta_{\min} = \frac{1}{2} \sin^{-1}\left(\frac{r_n m}{\pi r_0}\right) \tag{10}$$

with r_n denoting half the diameter of a single strand. Since the contact area calculated in the above equations is also that of flat strands, a scaling factor is used just like in [37]. However, while the scaling factor is empirically determined by Tondu, an attempt to quantify this factor can be found in their work, and the scaling factor is taken as the ratio of surface areas formed by two flat strands in contact to two spheres in contact. The contact between spheres is calculated using Hertz's contact theory and the final scaling factor is given as:

$$S^{(2)}_{\text{scale}} = \frac{r_n}{1.442\left[P_i r_n^3 \frac{(1-\nu_n^2)}{E_n}\right]^{\frac{1}{3}}} \tag{11}$$

where ν_n and E_n represent Poisson's ratio and Young's modulus of the braid strand, respectively. The modified expression for force takes the form:

$$F_{\text{Davis}} = \pi r_0^2 P_i \left[q_1 \left(1 - k_\epsilon \epsilon\right)^2 - q_2\right] \pm \mu_s P_i \left[\frac{S^{(2)}_{\text{contact}}}{S^{(2)}_{\text{scale}}}\right] \tag{12}$$

While Tondu added the correction factor term in the form of k_ϵ in Gaylord's equation, in [23], another correction term is added by Meller et.al. The force takes the form:

$$F_{\text{Meller}} = \pi r_0^2 P_i k_f^{(1)} \left[q_1 \left(1 - k_\epsilon^{(1)} \epsilon\right)^2 - q_2\right] \tag{13}$$

where the the newly added correction terms $k_f^{(1)}$ as well as $k_\epsilon^{(1)}$ are both determined as functions of input pressure as

$$k_f^{(1)} = k_{f(P_i)}^{(1)} = \frac{F_{\text{meas,max}(P_i)}}{\pi r_0^2 P_i \left(q_1 - q_2\right)},$$
$$k_\epsilon^{(1)} = k_{\epsilon(P_i)}^{(1)} = \frac{1}{\epsilon_{\text{meas,max}(P_i)}} \left(1 - \frac{1}{\sqrt{3}\cos\theta_0}\right)$$

The quantities $F_{\text{meas,max}} = \kappa_1 P_i + \kappa_2$ and $\epsilon_{\text{meas,max}} = \kappa_3 \ln(P_i)$ are calculated using curve fit on experimental data. This model is applied in the analysis of a climbing robot actuated using FAM in the work of Chapman et al. [40].

While the factors $F_{\text{meas,max}}$ and $\epsilon_{\text{meas,max}}$ contributed by Meller are empirical functions, in [41], Andrikopoulos et al. used constant values to these functions for simplicity. The expression for the force then takes the form

$$F^{(1)}_{\text{Andrikopoulos}} = \pi r_0^2 P_i k_f^{(2)} \left[q_1 \left(1 - k_\epsilon^{(2)} \epsilon\right)^2 - q_2\right] \tag{14}$$

where the factors $k_f^{(2)}$ and $k_\epsilon^{(2)}$ are not functions of pressure, but take the values

$$k_f^{(2)} = \frac{F_{\max}}{\pi r_0^2 P_{\text{test}} (q_1 - q_2)}, \quad k_\epsilon^{(2)} = \frac{l_0}{x_{\max}} \left(1 - \sqrt{q_2/q_1}\right)$$

To get the values of constants, a test pressure P_{test} is applied with zero end load to get the displacement $l_0 - l = x_{\max}$. Then $F_{\max}$ is the value of end force which will pull the actuator back to zero displacement position. Both quantities are experimentally determined.

2.3 Inclusion of material properties for bladder: linear elastic model

The earliest model which takes into account the material property of the bladder and thickness of the tube is probably that of Schulte [33] mentioned in the appendix of National Research Council's report on the application of external power in prosthetics and orthotics. The force according to this work is given by

$$\begin{aligned} F_{\text{Schulte}} &= \frac{b^2}{4\pi N^2} P_i \left(3\cos^2\theta - 1\right) \\ &+ \frac{bE}{N}\left[l_0 \sin\theta - \frac{\cos^2\theta}{\sin\theta}\left(\frac{b}{N}\sin\theta - 2\pi r_0\right)\right] \\ &- \frac{l_0 b}{N}\left(P_i - P_u\right)\left(\mu_s + \mu_{\text{st}}\right)\sin\theta \end{aligned} \tag{15}$$

The first term on the right hand side of the equation (15) represents the original pull equation by Gaylord. The second term is the resultant of considering the material properties of the bladder – the constant E being the Young's modulus of bladder material. The third term represents the friction force where P_u is the pressure required to inflate the unconstrained inner tube to a diameter equivalent to the device diameter at any value of θ and μ_{st} is the coefficient of friction between the braid and the tube. Many researchers have used this model in their study (see, for example, [42]) in a different form:

$$\begin{aligned} F_{\text{Ferraresi}} &= \frac{P_i}{4\pi N^2}(3l^2 - b^2) \\ &- Et_0 l\left(\frac{1}{N\sqrt{l^2 - b^2}} - \frac{1}{2\pi N^2 r_i}\right) + EA\left(\frac{l}{l_0}\right) \end{aligned} \tag{16}$$

where A is the cross sectional area of the cylinder.

This model by Ferraresi can also be seen in another format in the works of Kothera et al. [43]. The model derived in their paper, using force balance techniques, is essentially Chou's model which accounts for the thickness of bladder and Schulte's model which considers its linear elasticity. The force according to Kothera et al. is taken as

$$\begin{aligned} F_{\text{Kothera}}^{(1)} &= \frac{P_i}{4\pi N^2}\left(3l^2 - b^2\right) + P_i\left(\frac{V_b}{l} - \frac{tl^2}{2\pi r N^2}\right) \\ &+ EV_b\left(\frac{1}{l_0} - \frac{1}{l}\right) + \frac{El}{2\pi r N^2}(tl - t_0 l_0) \end{aligned} \tag{17}$$

From the experimental data shown in the works of Kothera et al., it is observed that modeling bladder as linear elastic material, even though this appears to be a simple approach, is fairly accurate. This is an interesting observation since this shows that the PAM operation is limited to within the linear regime of deformation of bladders which otherwise usually belong to hyper-elastic material category. Since determining accurate values for constants in non-linear models often require precise experimentation, linear material model may suffice for PAMs undergoing small deformation. However, if the material properties can be accurately described and if extensive computation can be afforded, then non-linear material modeling may provide better accuracy.

2.4 Inclusion of material properties for bladder: non-linear elastic model

If the bladder material is considered non-linear elastic, then obtaining analytical expressions of force using force-balancing techniques is difficult (if not impossible). The stress components are obtained from strain energy density functions and are directly used in the balance equations. In the paper by Delson et al. [44], the authors used a non-linear Mooney-Rivlin material ([45], [46]) to account for the elastic properties of the bladder. The strain energy density of a Mooney-Rivlin material takes the form:

$$\begin{aligned} W =& C_{10}\left(\lambda_1^2+\lambda_2^2+\lambda_3^2-3\right) \\ &+ C_{01}\left(\frac{1}{\lambda_1^2}+\frac{1}{\lambda_2^2}+\frac{1}{\lambda_3^2}-3\right) \end{aligned} \tag{18}$$

where

$$\lambda_1 = \frac{l}{l_0}, \lambda_2 = \frac{2r-t}{2r_0-t_0}, \lambda_3 = \frac{t}{t_0} \tag{19}$$

are the three stretch ratios. It may be noted that the median diameter is used in this formulation and the thickness is accounted for, unlike in the model used in [47], where the stretch ratios were defined assuming an incompressible material model and is given by

$$\lambda_1 = \frac{l}{l_0},\ \lambda_2 = \frac{r}{r_0},\ \lambda_3 = \frac{1}{\lambda_1\lambda_2} \tag{20}$$

The final expression for force is derived from the energy balance equation can be written as

$$\begin{aligned} F_{\text{Delson}} &= P_i\frac{dV}{dl} + V_b\frac{dW}{dl} \\ \text{and} \quad \pi lt(2r-t) &= \pi l_0 t_0(2r_0-t_0) \end{aligned} \tag{21}$$

where $V = \pi r^2 l$ is the volume occupied by the device and $V_b = \pi lt(2r-t)$ represents the volume of the bladder. Since the above equation cannot be directly integrated, a numerical integration scheme may be required for the solution.

The Mooney-Rivlin material model is also found in the work of Kothera et al. [43] where an energy balance method is used to derive the following expression for force:

$$\begin{aligned} F^{(2)}_{\text{Kothera}} &= \frac{P_i}{4N^2\pi}\left(3l^2-b^2\right) \\ &- V_b\Big(2C_{10}\left[\lambda_1\frac{d\lambda_1}{dl}+\lambda_2\frac{d\lambda_2}{dl}+\lambda_3\frac{d\lambda_3}{dl}\right] \\ &+ 2C_{01}\left[\lambda_1(\lambda_2^2+\lambda_3^2)\frac{d\lambda_1}{dl}+\lambda_2(\lambda_3^2+\lambda_1^2)\frac{d\lambda_2}{dl}\right] \\ &+ 2C_{01}\left[\lambda_3(\lambda_1^2+\lambda_2^2)\frac{d\lambda_3}{dl}\right]\Big) - \frac{P_i^2 b^3 l}{4\pi^2 m r_n E_b N^4} \end{aligned} \tag{22}$$

where the quantity E_b is the Young's modulus of braiding material. An application of this model can be seen in the works of Wereley's team [48] where PAM is used to produce large trailing edge flap in a helicopter. To this model, a friction force of the form $F_f = -\mu_f F_{\text{Kothera}}\text{sgn}(v)$ is added to Kothera's model where v is the tip velocity of PAM and the constant μ_f (which is not the coefficient of friction) is found out from experiments. It is worth noting that the authors suggest the use of derivations using force balance method [43] compared to energy balance method since the former was shown to have a better performance compared to the latter.

In [49], a neo-Hookean material [50] is assumed for the bladder which gives the strain energy density in terms of the stretch ratios as

$$W = \frac{E}{6}\left(\lambda_1^2+\lambda_2^2+\lambda_3^2-3\right) \tag{23}$$

Due to the relative simplicity in the material definition as opposed to the Mooney-Rivlin model, the authors could derive analytical expressions for pressure in terms of deformation as

$$P_i = \frac{E}{3}\left(\frac{r_0^2}{r_i^2} - 1\right) \times \frac{\begin{pmatrix}\lambda_1^8 \cos^4\theta_0 \cos 2\theta_0 - 2\lambda_1^6 \cos^2\theta_0 \cos 2\theta_0 \\ +\lambda_1^4 \cos 2\theta_0 + 2\lambda_1^2 \cos^2\theta_0 \cos 2\theta_0 \\ -\cos 2\theta_0 - 2\lambda_1^2 \cos^6\theta_0 + \cos^4\theta_0\end{pmatrix}}{\lambda_1^3\left(1 - 5\lambda_1^2 \cos^2\theta_0 + 7\lambda_1^4 \cos^4\theta_0 - 3\lambda_1^6 \cos^6\theta_0\right)} \tag{24}$$

From the above equation, for a given value of input pressure, the axial stretch ratio is calculated numerically. This is then used in the calculation of the axial force using the following formulation:

$$F_{\text{Trivedi}} = \pi E\left(r_0^2 - r_i^2\right)(\lambda_1 - 1) \tag{25}$$

The above expression however, makes the assumption that the material is linear elastic in the axial direction, which is inconsistent with the initial assumption.

Another description of static model considering Mooney-Rivlin material model can be found in [51]. In their model, the Hoop's force F_z and axial force F_θ acting on bladder during inflation are found analytically in terms of λ_1 and P_i. These values in conjunction with the static force balance equations from braid, gives the final expression for blocked force (applied load) as

$$F_{\text{Wang}} = F_z - P_i \pi r_i^2 - \frac{P_i r_i l^2 - F_\theta l^2}{2\pi N^2 r_o^2} \tag{26}$$

2.5 End-effects consideration

In the models described so far, the correction factor k_ϵ was used to take care of the effects of non-cylindrical ends. A few researchers have attempted to quantify this effect hoping to obtain better static characteristics of PAM. For example, in [52], the model developed considers the end-effect of PAM with ends modeled as conical frustums. The mathematical model derived takes the form:

$$\begin{aligned} F_{\text{Doumit}} =& m\left[\begin{array}{c}\left(\frac{P_i(r - t_0 - 2r_n) - \sigma_1 t_0}{mN\sin\theta}\right) l_{\text{cyl}} \\ +\left(\frac{P_i(r + r_c - 2t_0 - 2r_n)\cos\beta - 2\sigma_1 t_0}{mN\sin\left(\frac{\theta+\theta_c}{2}\right)}\right) l_{\text{cone}} \\ -\frac{P_i(r - 2r_n - t_0)^2}{2mr\cos\theta}\frac{l}{N}\tan\theta\end{array}\right] \\ & \times \cos\beta\cos\theta_c - P S^{(2)}_{\text{contact}}\mu_s \end{aligned} \tag{27}$$

The first term in the expression refers to the model taking into account the characteristics of conical ends while the second term is the frictional force component (σ_1 is the Hoop's stress on the bladder). The symbol l_{cyl} refers to the length of cylindrical section of PAM, l_{cone} refers to the slant length of conical frustum at the ends and r_c refers to the radius at the clamped end of the PAM. The quantity $S^{(2)}_{\text{contact}}$ is the effective area of contact between braids which is calculated by assuming the contact to be same as the contact between two cylinders and applying Hertz's contact theory. The validity and propriety of this assumption is, however, criticized in Tondu's review paper [32].

A more involved formulation for end tapering can be found in [30] where the force model used is the same as the one suggested by Ferraresi and found in [53] and [43]. At the ends, the bladder is assumed to take the shape of a section of elliptic toroid instead of conical frustum. The section of ellipse from $\pi/3$ radians to $\pi/2$ radians measured from the major axis is assumed to be the shape of PAM at the clamped ends. An expression relating the deformed radius of PAM with the eccentricity of ellipsoid is derived. Making use of this expression, a theoretical estimate for the length of a single strand of braid is formulated. By reducing

the error between the actual length of braid strand and numerically calculated value of the same for a given contracted length, the radius profile of deformed PAM is estimated. The obtained radius profile $f(z)$ at the outer surface is assumed to differ from the profile at the inner surface $g(z)$ by a constant thickness t. Then using incompressibility condition (the volume of bladder at rest and volume of bladder after deformation is same) the error between the initial and final volume is set to zero. This gave the final value of thickness of bladder and hence, the deformed shape of PAM. The estimate of thickness predicted from this approximation is compared with the models assuming fully cylindrical tips and is shown to have better conformation with results at higher contraction – where the end-effect is prominent.

2.6 Bladder as a thin walled tube

A few modeling attempts considering the bladder as a thin walled tube can also be found in the literature. In [54], the authors use large deformation theory on the deflation of a fiber-reinforced thin cylinder to determine the statics of PAM [55], [56]. To reflect the embedding of the nylon braiding cords, the stress resultant of thin cylinder is resolved as $\sigma_\alpha = \sigma_\alpha^1 + \sigma_\alpha^{11}$ where σ_α^1 is stress component due to deformation of bladder while σ_α^{11} is the stress component due to the braid strands. The solution procedure consists of guessing an initial value of the transverse stretch ratio λ_2 and iteratively adjusting the guess by comparing the value of initial length of tube obtained from formulation with the actual initial length. The closest choice of λ_2 will eventually predict the shape of outer surface of actuator and hence, the final deformed length. The main equations used are:

$$\begin{aligned} F_{\text{Liu}} &= 2\pi E r_0 \left(\frac{2\sigma_2(0)}{\lambda_2(0)} - \frac{P_i E}{r_0} \right), \\ l_0 &= -\int_{\lambda_2(0)}^{1} \frac{d\lambda_2}{\lambda_1 \sin\gamma(\lambda_2)} \end{aligned} \tag{28}$$

where the axial stress $\sigma_2(0)$ and radial stretch ratio $\lambda_2(0)$ are at the initial configuration and $\gamma(\lambda_2)$ is the angle made by the meridian of PAM (on the surface) with the z axis given as a function of the stretch ratio. However, it may be noted that in most PAMs, the fiber is not embedded inside the bladder, but forms a sheath on the outer surface. Hence, the application of this model on a general PAM structure is debatable.

Another model by Ball et al. [57] also considers thin wall approach in modeling PAM. In this case, the expression for force is given as

$$F_{\text{Ball}} = F_{\text{strands}} + F_{\text{pressure}} + F_{\text{elastic}} \pm \mu_f P_{\text{eff}} \tag{29}$$

where

$$\begin{aligned} F_{\text{strands}} + F_{\text{pressure}} &= \frac{P_o l^2}{2\pi N^2} - P_i \left(\frac{b^2 - l^2}{4\pi N^2} - \frac{V_b}{l} \right), \\ P_o &= P_i - \frac{\sigma_2 (r_0 - r_i)}{\lambda_1 \lambda_2 \sqrt{\frac{b^2 - l^2}{n^2 \pi^2} - \frac{4}{\pi}\frac{V_b}{l}}}, \quad F_{\text{elastic}} = \frac{\sigma_1 V_b}{l} \end{aligned} \tag{30}$$

with P_o as the pressure acting at the outer radius by the bladder on the sleeve and $\sigma_{1,2}$ is given in terms of material constants and stretch ratios. In case of thick walled bladder as well as pre-strained bladders, the thin wall tube model is applied sequentially as if the thick cylinder is an array of concentric nested thin tubes. The computational method calculates the pressure P_o of the innermost layer and works sequentially outwards. The derivations based on thin film approach on the same lines of [54] may also be found in the fiber-reinforced electro-pneumatic PAM shown in [58].

2.7 Advanced modeling of PAM

A few recently developed models try to capture the forces in PAM in greater detail. For example, in Chen et al. [59], two expressions for pressurization as well as the de-pressurization of a MPAM is derived. For pressurization, axial force is given as:

$$F_{\text{Chen}}^{(1)} = \frac{\pi P_i}{4}\left(\frac{b}{N\pi}\right)^2\left(3\cos^2\theta - 1\right) - \frac{4m^2N}{b\sin\theta}\left(M_f + M_d + M_r + M_{tr}\right) \tag{31}$$

For de-pressurization, the axial force is given as

$$F_{\text{Chen}}^{(2)} = \frac{\pi P_i}{4}\left(\frac{b}{N\pi}\right)^2\left(3\cos^2\theta - 1\right) + \frac{4m^2N}{b\sin\theta}\left(M_f - M_d - M_r + M_{tr}\right) \tag{32}$$

where the detailed expression for moments, M_f, M_d, M_r and M_{tr} represent the effects of friction between strands of threads, bending deformation of thread strand, bulging of bladder between the threads in braided sleeve and the friction between threads and bladder, respectively. The highly detailed model requires numerical integration tools and the accuracy of the model may depend heavily on the coefficients of friction between the braid strands, between the braid and tube as well as the guess on the contact surface area between the strands.

Another example is the description of statics in [41], where the model considers the effect of thermal expansion in PAM during actuation. The improved model from [41] takes the form:

$$\begin{aligned} F_{\text{Andrikopoulos}}^{(2)} = {} & \\ & \pi r_0^2 P_i k_f^{(2)}\left[q_1\left(1 - k_\epsilon^{(2)}(\epsilon + \alpha_l\Delta T)\right)^2 - q_2\right] \\ & - \left(\frac{2\pi r_0 l_0 \mu_s}{S_{\text{scale}}^{(1)}}\right)\times \\ & \frac{\sin\theta_0}{(1 - k_\epsilon(\epsilon + \alpha_l\Delta T))\sqrt{1 - \cos^2\theta_0(1 - k_\epsilon(\epsilon + \alpha_l\Delta T))^2}} \\ & \times P_i \text{sgn}\left(v\right) \end{aligned} \tag{33}$$

where α_l, ΔT and v represent the coefficient of thermal expansion of bladder, the change in temperature as well as the velocity of MPAM tip, respectively.

Apart from the usual methods which focus on finding an exact analytical expression to relate pressure, force and displacement of a PAM, a few models use numerical methods such as finite element methods to solve the statics of PAM. For example in [60], the authors use FEA to analyze the dynamics of PAM used in parachute systems. The preliminary model used is:

$$\epsilon = 1 - \sqrt{\frac{F\tan^2\theta_0}{2\pi r_0^2 P_i}} \tag{34}$$

where F is the applied force. The application of FEA can also be found in reference [61] as well as the analysis of a pneumatic bending fiber re-inforced actuator in reference [27]. Such analyses could be proven useful especially for actuators with non-uniform physical structure.

2.8 Modeling for MPAMs

In case of modeling miniaturized PAMs, thin walled tube approximation is not appropriate since the ratio between bladder material volume and the inner volume of bladder is usually high. Also, it has been found that many models for normal sized PAM need to be adjusted by adding correction factors so as to include the effects of forces which are difficult to measure. Reference [19] shows the analysis of a miniaturized FAM with outer diameter 1.5 mm and length between 22 mm and 62 mm intended to use in a fluidic actuated surgical tool. The equation for the force used is

$$\begin{aligned} &F_{\text{de Volder}} = \\ &\max\left[\left(F_{\min}, \frac{(P_i - P_{\text{i,corr}})b^2}{4\pi N^2}\right)\left(\frac{3(l-l_{\text{corr}})^2}{b} - 1\right)\right] \\ &+ \max\left[0, k_b\left(l - l_{b0}\right)\right] \end{aligned} \tag{35}$$

where l_{corr}, $P_{\text{i,corr}}$ are factors used to correct length and dead-band pressure, respectively. The term $F_{\min}$ is used as a threshold so that the PAM does not generate pushing forces. Finally, the term $k_b\left(l - l_{b0}\right)$ is added to generate a linear spring force equivalent in the model.

Another analysis and validation of statics of a MPAM with outer diameter between 3.02 mm and 4.19 mm is shown by Hocking et al. [53]. The basic force equation derived from Ferraresi has the Hoop's stress (σ_1) and axial stress (σ_2) terms which considers the elasticity of material [42]. The force is obtained as

$$F = \frac{P_i}{4\pi N}\left(3l^2 - b^2\right) + \sigma_1 \frac{V_b}{l} - \frac{\sigma_2 t l^2}{2\pi N^2 r} \tag{36}$$

In Hocking's paper, these stresses are considered as nonlinear (polynomial) functions of strain and the equation is modified as:

$$\begin{aligned} F^{(1)}_{\text{Hocking}} = &\frac{P_i}{4\pi N}\left(3l^2 - b^2\right) + \frac{V_b}{l}\sum_{i=1}^{n} E_i\left(\frac{l}{l_0} - 1\right)^i \\ &- \frac{tl^2}{2\pi N^2 r}\sum_{i=1}^{n} E_i\left(\frac{r}{r_0} - 1\right)^i \end{aligned} \tag{37}$$

where the material constants E_i are empirically identified from experimental results.

To the above model, friction is added as

$$F^{(2)}_{\text{Hocking}} = F^{(1)}_{\text{Hocking}} \pm \mu_f F^{(1)}_{\text{Hocking}} \text{sgn}(v) \tag{38}$$

One modification in the friction term compared to the other models is that, μ_f is assumed to vary with pressure. A dead-band pressure which is the threshold value of pressure upto which contraction does not start is usually observed in the case of MPAMs. In this paper, correction to account for dead-band pressure is made as $P_i^{\text{corr}} = P_i - P_c$ where P_c is calculated from experiments. Similarly, the tip effect is considered by using a corrected length, $L^{\text{corr}} = l - 2\left[\left(\frac{\pi}{2} - 1\right)(r - r_0)\right]$ in the above equation. A similar strategy is used in reference [3] where the model used is essentially that of Hocking [53] with the thickness term included from Chou's model [36]. In this model, the stress is empirically related to strain as a function of pressure as

$$\sigma = \sum_{j=1}^{n}\left(E_{jI} + E_{jS}P_i\right)\epsilon^j \tag{39}$$

where the constants are experimentally determined.

In another paper by Sangian et al. [62], the authors characterizes miniaturized FAM of outer diameter 5.6 mm taking into account the pressure dead-band. Gaylord's model is modified to include the threshold pressure ($\bar{P}_i$) required to initialize the contraction. The final force expression takes the form:

$$F_{\text{Sangian}} = \pi r_0^2 \left[q_1 \left(1-\epsilon\right)^2 - q_2 \right] \times \left[P_i - \bar{P}_i + \frac{E t_0 b}{2\pi N r_0^2} \left\{ \left(1 - \frac{l^2}{l_0^2} \cos^2\theta_0 \right)^{\frac{1}{2}} + \sin\theta_0 \right\} \right] \tag{40}$$

Use of empirical model formulation for MPAM (outer diameter 1.8 mm) can also be found in [26] where the static model used is

$$\epsilon_l = 1 - \sqrt{\frac{1}{\kappa_1}\left(\frac{F-\kappa_2}{P_i} - \kappa_3\right)} \tag{41}$$

$$\epsilon_r = \sqrt{\frac{\kappa_4 \epsilon_l^2 + \kappa_5 \epsilon_l + \kappa_6}{\kappa_6 \left(1-\epsilon_l\right)}} - 1 \tag{42}$$

2.9 Empirical considerations

As mentioned in section 1, advanced and more involved models are often quite difficult to implement in real-time control systems. Additionally, the measurement of exact values for parameters necessary for these advanced models will not be possible in all cases – it is hard to measure the deformed outer diameter of miniaturized muscles and axial strain of PAMs which are already employed in a robot. Hence, many models use empirical formulation derived from the basic models for practical purposes. In reference [5], the equation (6) is modified to obtain

$$F_{\text{Takosoglu}} = 4\pi r_0^2 P_i \left[q_1 \left(1-\epsilon\right)^n - q_2 \right] \tag{43}$$

the factor n and also the parameter q_1 are later empirically determined to be:

$$n(P_i) = \kappa_1 e^{\frac{-P_i}{\kappa_2}} + \kappa_3, \quad q_1(P_i) = \kappa_4 e^{\frac{-P_i}{\kappa_5}} + \kappa_6$$

In a model in reference [38] the expression is further empirically adjusted to:

$$F_{\text{Itto}} = \pi r_0^2 P_i \left[q_1 \left\{ 1 - \kappa_1 \left(1 + e^{\kappa_2 P_i} \right) \epsilon \right\}^2 - q_2 \right] \tag{44}$$

and the above model so formed is seen to agree well with experimental values.

In reference [16], the authors analyze the static model of a PAM used as 'pedestrian dummy device' in the test set up of pedestrian safety system. The model derived takes the form:

$$F_{\text{Doric}} = F_{\text{Chou}} - F_{\text{PAM, e}} - F_{\text{PAM, s}} \tag{45}$$

$$\text{where} \quad F_{\text{PAM, e}} = \left(1 - \frac{w}{w_0}\right)\kappa_1, \quad F_{\text{PAM, s}} = \frac{P\epsilon}{l_0}\kappa_2$$

The second and third terms take into account the effects of thickness, elasticity of bladder as well as the form of PAM. The correction factors for elasticity as well as the shape of PAM, κ_1 and κ_2 are experimentally determined.

Purely empirical formulations are also presented in the works of [15], [63], [64], [65], [66] and [67] for its relative ease in control system design. In these papers, the empirical expressions for blocked force as a

function of applied pressure and axial strain take different forms such as

$$F(P_i,\epsilon) = (\kappa_1 + \kappa_2\epsilon + \kappa_3\epsilon^2)P_i + (\kappa_4 + \kappa_5\epsilon + \kappa_6\epsilon^2 + \kappa_7\epsilon^3 + \kappa_8\epsilon^4) \quad (46)$$

$$F(P_i,\epsilon) = \kappa_1 + \kappa_2\epsilon + \kappa_3\epsilon^2 + \kappa_4 P_i + \kappa_5\epsilon P_i \quad (47)$$

$$F(P_i,\epsilon,\dot{\epsilon}) = \left(\kappa_1 P_i^2 + \kappa_2 P_i + \kappa_3\right)\epsilon + \kappa_4 P_i + \kappa_5 + \kappa_6\dot{\epsilon} \quad (48)$$

$$F(\epsilon) = \kappa_1 F_{\max}(1 - \frac{\epsilon}{\epsilon_{\max}}) \quad (49)$$

where constants κ are determined from prior experimentation.

2.10 Modeling hysteresis

In almost all the models described in the previous section, hysteresis is accounted by adding or subtracting a frictional force term to the static equation for axial force. A convincing representation of the added frictional force term is not yet developed to the best of our knowledge. In most cases, an approximating function is chosen to represent this frictional force term which is empirically determined. For example, in [30], this additional frictional force term F_{fstat} is calculated from the static force term F_{stat} obtained from phenomenological models as

$$F_{\text{fstat}} = -\mu_f F_{\text{stat}} = (\kappa_1 + \kappa_2 P_i)\, F_{\text{stat}} \quad (50)$$

While the term F_{stat} gives the mean curve of force-deformation plot, adding or subtracting this frictional force term will give the pressurizing and the de-pressurizing curve. In the above equation, the coefficient of friction is assumed to be linearly dependent on applied pressure and the constants k_1 and k_2 are determined from experiments.

In a few research works, empirical formulations are derived for force-displacement curves for expansion and compression of a PAM in a manner different from the method mentioned above. In cases where accurate hysteresis modeling is required– especially for practical applications, force-length and pressure-length hysteresis profiles of PAM are found out for compression and expansion curves separately. For example, in [68], van Damme et al. derived a hysteresis profile for pleated PAM using Preisach hysteresis model [69]. The math model takes the form

$$F_{\text{hyst}} = P_i l_0^2 f_{t_0}^{\text{fit}} \left(1 + \kappa_{\text{scale}} \left(W[\epsilon_s] - W_{(\epsilon_s)}^{\text{fit}}\right)\right) \quad (51)$$

where $f_{t_0}^{\text{fit}} = \kappa_0\epsilon^{-1} + \kappa_1 + \kappa_2\epsilon + \kappa_3\epsilon^2 + \kappa_4\epsilon^3$ is the approximated mean curve of force-displacement hysteresis. The function $W_{[\epsilon_s]}$ is the output of Preisach model which is a weighted summation of small discrete hysteresis relays and the function $W_{(\epsilon_s)}^{\text{fit}}$ represents a curve fitted between the two curves generated by $W_{[\epsilon_s]}$ and κ_{scale} is a scaling factor. The proposed model is shown to estimate hysteresis phenomenon in PAM for contractile range below 20%.

A Maxwell slip model [70] for hysteresis is described in references [71], [72]. In this method, the force-length hysteresis of the PAM – the hysteresis component in PAM force curve due to the motion of PAM as well as the stretching of bladder – is experimentally determined and modeled. In order to achieve this, at first the force is measured from a constrained model where the motion of PAM is arrested. Then isobaric experiments are carried out where the pressure is kept constant and force value corresponding to change in length is obtained. The difference between the two values gives the force-length hysteresis in PAM. This component of hysteresis appears to be qualified as 'non-local memory hysteresis' which can be modeled using Maxwell slip model. In non-local memory hysteresis modeling, when the PAM is actuated towards a particular contracted length (following a particular force-length curve) and is allowed to dilate (following a different curve), by 'remembering' the parameters of return points (F_m and ϵ_m), the subsequent contraction

and dilation can be modeled by knowing the characteristic curve called the 'virgin curve'. In mathematical form, this procedure can be written as:

$$F_{\text{hys}} = F_{\text{m}} + 2f((\epsilon - \epsilon_m)/2);$$
$$f = y(\epsilon), v \geq 0, \quad f = -y(-\epsilon), v \leq 0 \tag{52}$$

where $y(\cdot)$ represents the virgin curve. In their papers, this virgin curve is identified as piecewise linear curve. For each piece of the curve, a slip element with stiffness 'k' and maximum saturation force 'w' can be attributed. The piecewise continuous stiff elements can also be visualized as a parallel arrangement of spring systems with each element having different values of stiffness and a saturation force limit (representing the pressure in pressure-length hysteresis plot) beyond which displacement does not take place for that particular element. From the knowledge of each slip elements, the hysteretic force can be calculated for any choice of length, by intuitively choosing the right number of elements that would contribute to the section of curve. The total hysteresis force, F_{hys}, is the sum $\sum_1^n F_i$.

In another paper by Jin et al. [73], the authors show a Bouc-Wen model [74] to represent the pressure-length hysteresis of PAM for use in control system design. In this work, the hysteresis loop for pressure-length curve is represented using the expression:

$$l(t) = k(k_1 P_i(t) - h(t)) + \rho \tag{53}$$

where $h(t)$ is a solution of the equation

$$\dot{h} = \alpha \dot{P}_i(t) - \gamma \dot{P}_i(t)|h|^n - \beta z|\dot{P}_i(t)||h|^{n-1} \tag{54}$$

with the parameters n, k, k_1, ρ, α, β, γ identified by minimizing the least square error between the model and experimental data. The paper also presents a Prandtl-Ishlinskii (PI) [75] model for pressure-length hysteresis representation where the loop is given by the equations:

$$l(k) = \mathbf{w}^T \mathbf{H}_r[P_i, l_0](k) =$$
$$\sum_{i=0}^{n-1} w_i \cdot \max\{P_i(k) - r_i, \min\{P_i(k) + r_i, l(k-1)\}\} \tag{55}$$

In the above $\mathbf{H}_r$ are the backlash (play) operators of PI model and k is the sampling number of the operator. The weights w_i and threshold r_i are found out using least square error minimization as mentioned in the case of Boruc-Wen model. The application of Prandtl-Ishlinki model on trajectory control of PAM can be found in [76] (see also [77]).

The models suggested in [73], however are suitable mostly for symmetric hysteresis loops. In [78], a modification to this model which can be used in asymmetric hysteresis loop is proposed. Here, in the basic PI model, the backlash operator is divided into two, one for ascending and one for descending curves and is written as

$$l(t) = \kappa_1 P_i(t) + \sum_{i=1}^{n} w_i^a (\mathbf{H}_{ri}^a[P_i, l_0](t) - P_i(t))$$
$$+ \sum_{i=1}^{n} w_i^d (\mathbf{H}_{ri}^d[P_i, l_0](t) - P_i(t)) \tag{56}$$

where $\mathbf{H}_{ri}^{a,d}$ are different for ascending and descending; κ_1 is a constant. The two operators are subject to constraints:

$$\mathbf{H}_{ri}^a[1, l_0](t) = 1, \quad \mathbf{H}_{ri}^a[1, l_0](k) = 1,$$
$$\kappa_1 + \sum_{i=1}^{n} w_i^a \mathbf{H}_{ri}^a[1, l_0](t) + \sum_{i=1}^{n} w_i^d \mathbf{H}_{ri}^d[1, l_0](t) = 1$$

In the above there are $(2n+3)$ parameters that need to be identified – the additional 3 parameters compared to the classic PI model are from determining coefficients of a quadratic function used in the descending play operator. Another variant in PI hysteresis model is shown in [79] where an 'Extended Unparallel PI' model is proposed. Here, the PI model is modified so that the ascending and descending edges are multiplied with factors α and β, which change the respective slopes. The final backlash operator becomes:

$$\begin{aligned}\mathbf{H}_{r_i,\alpha_i,\beta_i[P_i](k)} = \max\{&\alpha_i(P_i(k)-r_i),\\ &\min\left\{\beta_i(P_i(k)+r_i), \mathbf{H}_{r_i,\alpha_i,\beta_i[P_i](k-1)}\right\}\}\end{aligned} \tag{57}$$

2.11 Summary of models in literature

The improvement put forward by different phenomenological models in literature from the basic model by Gaylord and the key equations used in the same is shown in Table 1. Table 2 compares the major modeling considerations in the models. The models shown in rows marked with * are experimentally validated in literature on miniaturized versions of PAMs or FAMs. From the earlier part of this section, we see that most of the models for MPAMs require prior experimentation to accurately determine the correction factors, friction coefficients as well as the empirical constants used in the stress equations. The simpler model proposed by Sangian et al. (equation (40)) is quite inaccurate in predicting the pressure-deformation characteristics of MPAM as shown in the later section of this paper, while the numerical iterative method used by Ball et al. is computationally expensive and non-trivial to implement. Moreover, it is also observed by the authors that many models proposed in the literature are inconsistent to the changes in initial parameters when applied on MPAMs. For measurements taken from specimens belonging to same fabricated lot, the accuracy of theoretical models vary considerably when only the initial length or braid angle is different, while keeping all the other material and fabrication parameters constant. This anomaly and the gap in literature necessitates the development of an improved statics model for MPAM. Additionally, as shown in the next section, numerical solutions of the various models do not match very well with experimental results of MPAMs (see figures 13 and 14 in Section 4). In the subsequent section, we propose a new approach to model the statics of MPAM, which is shown to be consistent with variation in MPAM parameters and in reasonable agreement with experiments done on MPAMs.

3 Proposed model for MPAM

In this section, we introduce a novel phenomenological approach in modeling statics of MPAM. Before the modeling is discussed in detail, characteristics of the MPAMs fabricated as well as the set-up used for experimentation is discussed.

3.1 Fabricated MPAM characteristics

In our study, we use two MPAMs consisting of an inner silicone tube with $r_o = \{0.55, 0.75\}$ mm, $r_i = \{0.25, 0.25\}$ mm braided on the outer surface using nylon cords of radius $\sim 50\mu m$ at an angle of $\alpha = \{36°, 38°, 40°\}$ (refer figure 2). Since the angle of winding is less than 54.7°, the actuator contracts upon application of pressure [36]. The overall outer diameter of MPAM is 1.2 mm and 1.6 mm. For braiding, we used a standard Horn gear braiding machine used in the fabrication of coaxial communication cables. Most commercially available braiding machines are designed for braiding the tubes up to a minimum of 5 mm. However, by manually adjusting the configuration of machine, it was possible to braid the silicone tube so that the gap between silicone tube and braid is minimized. In spite of the care taken during fabrication, in the MPAMs used for experiments, there exist a small gap δ between the outer radius of the silicone tube r_o and the inner surface of braid with the radius r_b. The fabrication process also limits the range of helix angles with which the nylon fibers could be braided – in the fabricated MPAMs we could get helix angles

Author	Key equation(s)	Important considerations
Gaylord [1]	$F = \frac{b^2}{4\pi N^2} P_i \left(3\cos^2\theta - 1\right)$, eq. (3)	Kinematics of braid
Schulte [33]	$F = \frac{b^2}{4\pi N^2} P_i \left(3\cos^2\theta - 1\right) + \frac{bE}{N}\left[l_0 \sin\theta - \frac{\cos^2\theta}{\sin\theta}\left(\frac{b}{N}\sin\theta - 2\pi r_0\right)\right]$	
	$-\frac{l_0 b}{N}\left(P_i - P_u\right)\left(\mu_s + \mu_{\text{st}}\right)\sin\theta$, eq. (15)	Inclusion of material properties
Chou [36]	$F = \frac{b^2}{4\pi N^2} P_i \left(3\cos^2\theta - 1\right) + \pi P_i \left[\frac{bt_0}{N\pi}\left(2\sin\theta - \frac{1}{\sin\theta}\right) - t_0^2\right]$, eq. (5)	Thickness of bladder
Tondu [37]	$F = \pi r_0^2 P_i \left[q_1 \left(1 - k_\epsilon \epsilon\right)^2 - q_2\right] \pm \mu_s P_i \left[\frac{S^{(1)}_{\text{contact}}}{S^{(1)}_{\text{scale}}}\right]$, eq. (8)	End-effects and friction term
Ferraresi [42]	$F = \frac{P_i}{4\pi N}\left(3l^2 - b^2\right) + \sigma_1 \frac{V_b}{l} - \frac{\sigma_2 t l^2}{2\pi N^2 r}$, eq. (36)	Inclusion of Hoop and axial stress
Liu [54]	$F = 2\pi E r_0 \left(\frac{2\sigma_2(0)}{\lambda_2(0)} - \frac{P_i E}{r_0}\right), \quad l_0 = -\int_{\lambda_2(0)}^{1} \frac{d\lambda_2}{\lambda_1 \sin\gamma(\lambda_2)}$, eq. (28)	Iterative procedure
Delson [44]	$F = P_i \frac{dV}{dl} + V_b \frac{dW}{dl}$, eq. (21)	Non-linear elastic material
Davis [39]	$F = \pi r_0^2 P_i \left[q_1 \left(1 - k_\epsilon \epsilon\right)^2 - q_2\right] \pm \mu_s P_i \left[\frac{S^{(2)}_{\text{contact}}}{S^{(2)}_{\text{scale}}}\right]$, eq. (12)	Improved friction term
Trivedi [49]	$F = \pi E\left(r_0^2 - r_i^2\right)\left(\lambda_1 - 1\right)$, eq. (25)	Neo-Hookean material model
Doumit [52]	$F = m\cos\beta\cos\theta\left[\left(\frac{P_i(r - t_0 - 2r_n) - \sigma_1 t_0}{mN\sin\theta}\right) l_{\text{cyl}} - \frac{P_i(r - 2r_n - t_0)^2}{2mr\cos\theta}\frac{l}{N}\tan\theta\right.$	
	$\left. + \left(\frac{P_i(r + r_c - 2t_0 - 2r_n)\cos\beta - 2\sigma_1 t_0}{mN\sin\left(\frac{\theta+\theta_c}{2}\right)}\right) l_{\text{cone}}\right] - P S^{(2)}_{\text{contact}}\mu_s$, eq. (27)	Improved end-effect term
de Volder* [19]	$F = \max\left[\left(F_{\min}, \frac{(P_i - P_{\text{i,corr}})b^2}{4\pi N^2}\right)\left(\frac{3(l - l_{\text{corr}})^2}{b} - 1\right)\right] + \max\left[0, k_b\left(l - l_{b0}\right)\right]$,eq.(35)	Model for MPAM
Hocking* [53]	$F = \frac{P_i}{4\pi N}\left(3l^2 - b^2\right) + \frac{V_b}{l}\sum_{i=1}^{n} E_i \left(\frac{l}{l_0} - 1\right)^i - \frac{tl^2}{2\pi N^2 r}\sum_{i=1}^{n} E_i \left(\frac{r}{r_0} - 1\right)^i$, eq. (37)	Polynomials for stress and strain
Chen [59]	$F = \frac{\pi P_i}{4}\left(\frac{b}{N\pi}\right)^2\left(3\cos^2\theta - 1\right) \mp \frac{4m^2 N}{b\sin\theta}\left(M_f \pm M_d \pm M_r + M_{tr}\right)$, eq. (31),(32)	Improved friction terms
Wang [51]	$F = F_z - P_i \pi r_i^2 - \frac{P_i r_i l^2 - F_\theta l^2}{2\pi N^2 r_o^2}$, eq. (26)	Using Mooney-Rivlin model
Robinson [30]	Same as Ferraresi, eq. (16)	Elliptical shape for end
Pillsbury* [3]	$\sigma = \sum_{j=1}^{n}\left(E_{jI} + E_{jS} P_i\right)\epsilon^j$,, eq. (39)	Pressure dependent stress term
Sangian* [62]	$F = \pi r_0^2 [q_1(1 - \epsilon^2) - q_2] \times$	
	$\left[P_i - P_{\text{th}} + \frac{E t_0 b}{2\pi N r_0^2}\left\{\left(1 - \frac{l_0^2}{l_0^2}\cos^2\theta_0\right)^{\frac{1}{2}} + \sin\theta_0\right\}\right]$, eq. (40)	Threshold pressure deadband
Andrikopoulos [41]	$F = r_0^2 P_i k_f^{(2)}\left[q_1\left(1 - k_\epsilon^{(2)}(\epsilon + \alpha_l \Delta T)\right)^2 - q_2\right]$	
	$-\left(\frac{P_i \text{sgn}(v)}{S^{(1)}_{\text{scale}}}\right)\frac{2\pi r_0 l_0 \mu_s \sin\theta_0}{(1 - k_\epsilon(\epsilon + \alpha_l \Delta T))\sqrt{1 - \cos^2\theta_0 (1 - k_\epsilon(\epsilon + \alpha_l \Delta T))^2}}$, eq. (33)	Temperature effects on PAM
Ball* [57]	$F = F_{\text{strands}} + F_{\text{pressure}} + F_{\text{elastic}} \pm \mu_f P_{\text{eff}}$, eq. (29)	Concentric thin walled tubes

Table 1: Summary of phenomenological models of PAM. (* applied to miniaturized PAMs/FAMs)

between 36° and 40°. The actual fabricated MPAMs are shown in Figure 2. It maybe mentioned that the ends are larger as an epoxy adhesive is applied to seal the ends for experimentation.

The layout of pneumatic circuit used to actuate MPAM is shown in Figure 3. A pneumatic compressor of maximum output pressure 1034 kPa (150 psi) is connected to a 1 liter air (at NTP) reservoir which is used to deliver high pressure air to the MPAM. A pressure regulating circuit operates the compressor when the value of pressure in reservoir falls below certain threshold thereby maintaining availability of 827 kPa (120 psi) pressure at all times. Two proportional valves are used to control pressure inside air muscle – one

Author (year) [ref.]	Basic equation	Correction factors	Linear elastic material	Non-linear elastic material	End considerations	Thin tube	Advanced modelling	MPAMs	Friction term
Schulte (1961) [33]	✓		✓						✓
Tondu (2000) [37]	✓	✓			✓				✓
Ferraresi (2001) [42]	✓		✓						✓
Liu (2003) [54]				✓		✓			
Delson (2005) [44]				✓			✓		✓
Zang (2005) [60]				✓		✓	✓		
Davis (2006) [39]	✓	✓			✓				✓
Trivedi (2008) [49]				✓			✓		
Kothera(a) (2009) [43]	✓		✓						✓
Kothera(b) (2009) [43]				✓			✓		✓
Doumit (2009) [52]					✓		✓		✓
de Volder (2011) [19]	✓	✓						✓	
Hocking (2012) [53]	✓	✓		✓				✓	✓
Chen (2014) [59]			✓				✓		✓
Robinson (2015) [30]	✓		✓		✓				✓
Meller (2015) [23]	✓	✓							
Sangian (2015) [62]	✓	✓	✓					✓	
Pillsbury (2015) [3]	✓			✓				✓	
Wang (2015) [51]				✓			✓	✓	✓
Ball (2016) [57]			✓			✓	✓		✓
Andrikopoulos (2016) [41]	✓	✓	✓				✓		✓

Table 2: Comparison between different phenomenological models

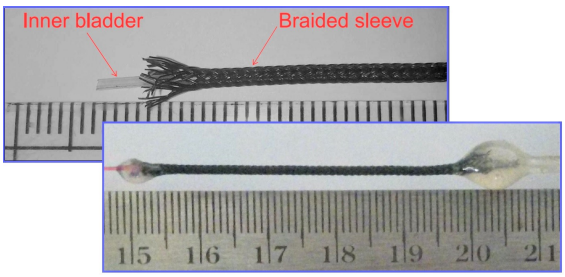

Figure 2: Fabricated MPAM – 1.5 and 1.2 mm diameter

for pressurizing the MPAM and the other for bleeding. A Honeywell pressure transducer (with range of 0 to 1034 kPa) is connected in series with MPAM to measure the inner pressure. An ATmel ATMega2560 micro-controller board interfaced with MATLAB controls the proportional valves through a current driver circuit to maintain user defined value of pressure inside the MPAM. To keep a straight alignment of the MPAM, a 5 gram weight is applied on the free end. For a 40 mm air muscle, the maximum deformation of 15 gram end-loading varies from 5 gram by less than 0.3 mm (less than 3% of total deformation). Since

this variation in deformation is comparable to the error bounds of the measurements in the experiments, the effect of this small end-loading is ignored in the formulations. The experimental set-up used is shown in Figure 4[1].

The deformation of MPAM is captured using a high resolution camera and changes in length are computed using image processing. The measurement method consists of taking images of MPAMs in its operational state using high resolution camera and identifying the length of MPAM by measuring the displacement between the image pixels corresponding to the tips of MPAM. At first, size of each pixel in the HD camera image is calculated based on a benchmarking with a standard object with known dimensions. Then the distance between two markers set in the either ends of MPAM is calculated in terms of pixels and using the scale mentioned above, it is converted in terms of millimeters. The possible error in this method is in identifying the marker pixels which is not more than 2 pixels size in each ends. For the scale and measurement set up used, this value is about 0.2 mm. We have also carefully avoided any perspective issues in measurement, by conducting the scale determination as well as the MPAM operation in the same focal plane of camera. All measurements are repeated more than 5 times and the results are reported as mean of the obtained vales and measurement errors shown in error bars.

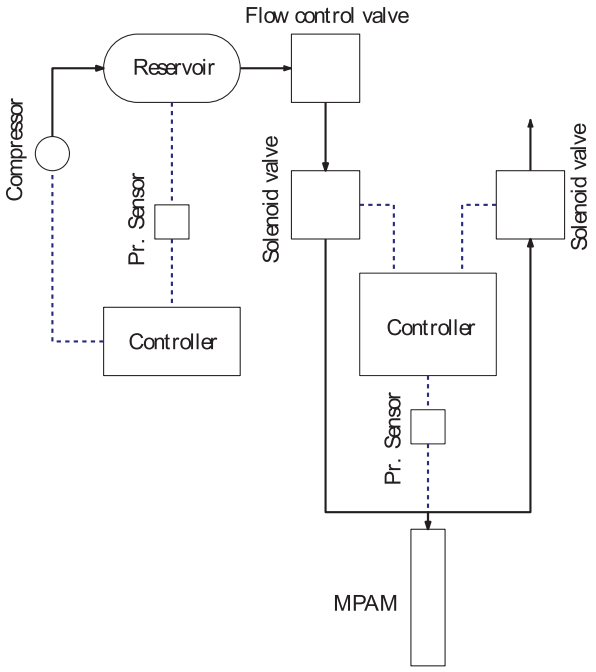

Figure 3: Layout of pneumatic circuit and controller

Figure 5 shows the end-point displacement of MPAM during inflation as well as deflation with dead load ($F = 0.05N$) attached at the end. The MPAM clearly shows hysteresis. The maximum error due to measurement is about 0.1 mm and error bars in the plot are obtained from at least 5 sets of experiments. In the comparisons with existing approaches, the hysteresis is not shown and the mean value, between the inflation and deflation, is used (see figure 5). We performed experiments with a 40 mm MPAM and a 60 mm MPAM using the experimental setup described above and compared the experimental results with theoretical values obtained from various models available in literature – see Figure 6 and Figure 7. Since our focus is on identifying the mechanics of MPAM, the comparison plots are limited to only phenomenological models as opposed to the models which rely on empirical data as well as parameters which require sophisticated measurement set-up for identification. Also, models which can be easily implemented and do not use

[1]In the actual experiments, the MPAM is positioned vertically with a weight of 5 grams hanging on the free end. The horizontal position shown in figure is for better visualization.

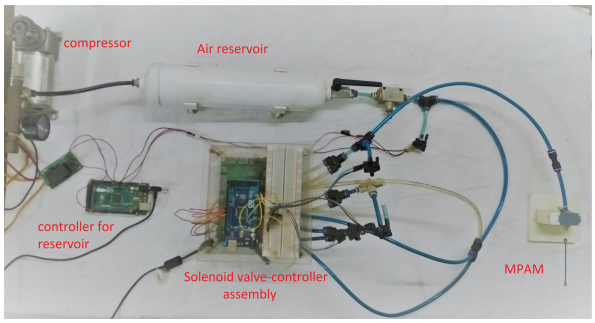

Figure 4: Experimental set-up

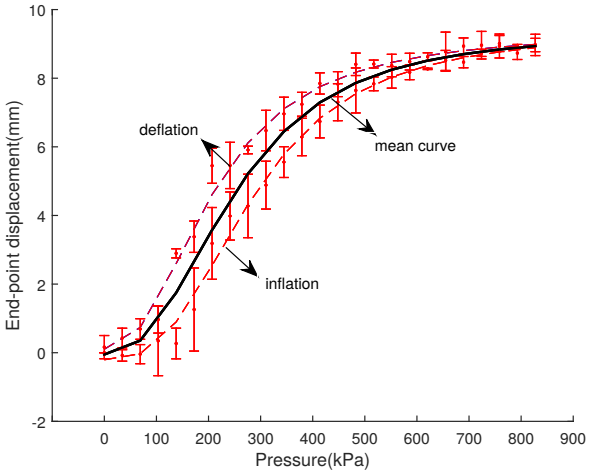

Figure 5: Hysteresis observed in MPAM

correction factors are only considered. The MPAMs used for validation have same physical characteristics and differ only by their lengths. We can see that except Hocking's model, other models are not accurate when predicting the deformation of fabricated MPAM keeping all the parameters constant except the initial length. Even though Hocking's model is able to predict the unloaded displacement accurately, it gives large error when predicting the stiffness of a pressurized MPAM (actual stiffness is about 10 times larger than the predicted stiffness value).

3.2 Statics model for MPAM

3.2.1 Characterization of pressure dead-band

In figure 8, we can see the pressure deadband which is the range of pressure below which contraction of MPAM is not apparent. This pressure deadband is mentioned in [53] as due to the Mullin's effect, which is unlikely in the case of MPAM used in this work. In our case, the MPAM was pre-stretched and inflated multiple times, so as to form a permanent set before it is braided on the outer surface. This ensured the repeatability of bladder inflation characteristics while employed in the MPAM. It is also observed that the un-braided bladder inflates considerably at values of pressure within this dead-band range. On closer observation, it is found that the MPAM expands instead of contracting in this range (see inset of figure 8) and this is due to the small gap δ (of the order of 0.04 mm) between the tube and nylon sleeve during fabrication, as mentioned in earlier section. It may be noted that this expansion is not usually seen in commercial PAMs as well as fiber

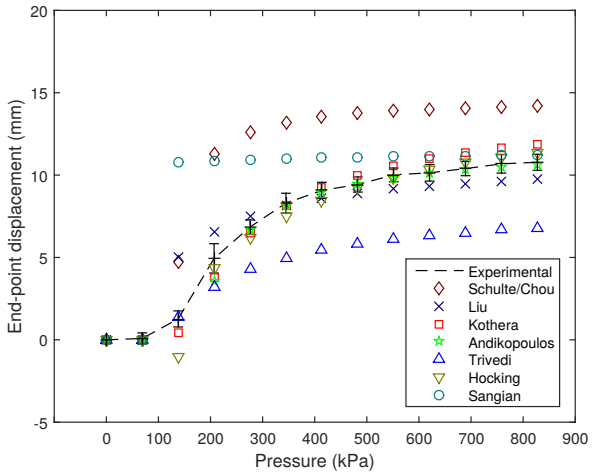

Figure 6: End-point displacement vs applied pressure for 40 mm MPAM. $\theta_0 = 36°$, $r_i = 0.25$ mm, $r_o = 0.55$ mm, $r_n = 0.04$ mm, $m = 30$, $\phi = 5$mm, $E = 0.35$ MPa, $\nu = 0.499$, $F = 0.05$ N.

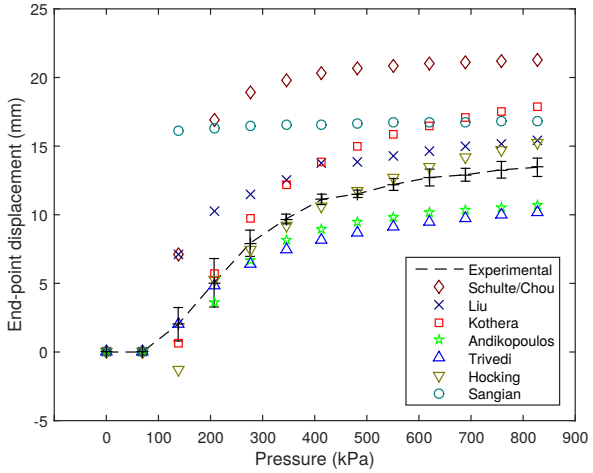

Figure 7: End-point displacement vs applied pressure for 60 mm MPAM. $\theta_0 = 36°$, $r_i = 0.25$ mm, $r_o = 0.55$ mm, $r_n = 0.04$ mm, $m = 30$, $\phi = 5$mm, $E = 0.35$ MPa, $\nu = 0.499$, $F = 0.05$ N.

embedded PAMs where this gap is unlikely to occur while it was prominent in the fabricated braided sleeve PAMs as in the case of the MPAM used in this work and in the work presented in [53]. Due to this gap, the initial stage of pressurization results in the expansion of silicone tube till the outer surface of silicone tube makes contact with the nylon sleeve. The pressure at which contact occurs is termed the critical dead-band pressure $\bar{P}_i$. Since the forces acting on MPAM before and after the critical deadband pressure are different, we consider this as two phases of contraction which has to be treated separately. We assume the bladder material as linear elastic for simplicity in derivations and also since the linear elastic model is shown to be sufficient to capture model characteristics as observed from Kothera's model [43].

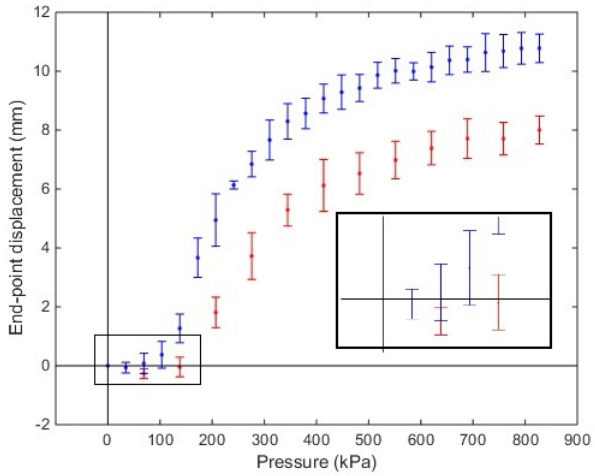

Figure 8: Deformation phases of MPAM (inset – elongation part zoomed)

3.2.2 Model for first phase–expansion

In the first phase of deformation, the bladder expands without the constraint of the outer braid sheath. In this phase, we use the linear thick cylinder approach to find the displacements in axial and radial directions. The equilibrium equations for inflation of thick cylinder are given by [80]

$$\frac{\partial}{\partial r}\left(\frac{1}{r}\frac{\partial(ru_r)}{\partial r}\right) = 0, \quad \frac{\partial^2 u_z}{\partial z^2} = 0 \tag{58}$$

where u_r and u_z are the displacements of silicone tube in radial and axial directions, respectively[2]. Solving the equations, we get the displacements

$$u_r = c_1 r + \frac{c_2}{r}, \quad u_z = c_3 z + c_4 \tag{59}$$

where $c_i,\ i = 1, 2, 3, 4$ are constants. In the initial phase of deformation, since the braid has not come in contact with the tube, the outer surface will be pressure free. The applied pressure P_i will act in the inner cylindrical surface while in the axial ends, inflation pressure as well as the pressure due to applied axial load will act. This pressure component will be $P_s = P_i \frac{r_i^2}{r_o^2 - r_i^2} + P_{\text{sil}}$, where P_{sil} is the pressure acting on the silicone tube due to the applied axial load F. Using these boundary conditions as well as the zero

[2]The variable r in this section would represent the radial co-ordinate in the cylindrical co-ordinate system as opposed to the deformed outer radius of tube in section 2

displacement condition on the fixed end of the MPAM, we get the values of constants as:

$$
\begin{aligned}
c_1 &= \frac{(\Lambda_1 + 2\Lambda_2)}{2\Lambda_2\,(3\Lambda_1 + 2\Lambda_2)} \times \\
&\quad \left[\frac{P_i r_i^2}{r_o^2 - r_i^2} + \frac{P_o r_o^2}{r_o^2 - r_i^2} - \frac{P_s \Lambda_1}{\Lambda_1 + 2\Lambda_2}\right] \\
c_2 &= \frac{1}{2\Lambda_2}\left[\frac{r_i^2 r_o^2}{r_o^2 - r_i^2}\right](P_i - P_o) \\
c_3 &= \frac{\Lambda_1}{\Lambda_2\,(3\Lambda_1 + 2\Lambda_2)} \times \\
&\quad \left[-\frac{P_i r_i^2}{r_o^2 - r_i^2} + \frac{P_o r_o^2}{r_o^2 - r_i^2} + P_s \frac{\Lambda_1 + \Lambda_2}{\Lambda_1}\right] \\
c_4 &= 0
\end{aligned} \tag{60}
$$

where Λ_1 and Λ_2 are Lame's parameters. Substituting the constants, we get the displacements as:

$$
\begin{aligned}
u_r|_{r=r_o} &= \frac{r_o}{\Lambda_2\,(3\Lambda_1 + 2\Lambda_2)} \times \\
&\quad \left[\frac{2\,(\Lambda_1 + \Lambda_2)\,r_i^2}{(r_o^2 - r_i^2)} P_i - \frac{\lambda}{2}\left(P_i \frac{r_i^2}{r_o^2 - r_i^2} + P_{\text{sil}}\right)\right]
\end{aligned} \tag{61}
$$

$$
\begin{aligned}
u_z|_{l=l_0} &= \frac{\Lambda_1 l_0}{\Lambda_2\,(3\Lambda_1 + 2\Lambda_2)} \times \\
&\quad \left[-\frac{P_i r_i^2}{r_o^2 - r_i^2} + \left(P_i \frac{r_i^2}{r_o^2 - r_i^2} + P_{\text{sil}}\right)\frac{\Lambda_1 + \Lambda_2}{\Lambda_1}\right]
\end{aligned} \tag{62}
$$

The MPAM expands according to the above equations till the tube makes contact with the braid. The pressure components at this point remains the same as that of the initial expansion phase, since there is no radial pressure on the outside surface of the silicone tube at the onset of contact. As the tube expands, the braid deforms as per the kinematics rule given in equations (1) and (2). Taking into account the gap between braid and the tube, the modified kinematics model of the braided sleeve can be written as:

$$l_0 = b\cos\theta_0, \quad 2\pi r_b N = b\sin\theta_0 \tag{63}$$

$$l_0 + \hat{u}_z = b\cos\theta, \quad 2\pi(r_b + \hat{u}_r)N = b\sin\theta \tag{64}$$

where $r_b = r_0 + \delta$ is the initial radius of the braided sleeve and the quantities $\hat{u}_r$ and $\hat{u}_z$ represent the radial as well as the axial displacements of the braided sleeve. The above equations can also be written as a single expression which relates the radial and axial displacements of the sleeve:

$$\hat{u}_r = r_b\left\{\frac{1}{\sin\theta_0}\sqrt{1 - \cos^2\theta_0\left(1 + \frac{\hat{u}_z}{l_0}\right)^2} - 1\right\} \tag{65}$$

Since the braid and sleeve are sealed at the tips, the axial displacement of the sleeve and the tube is the same. Hence, $\hat{u}_z = u_{z(l=l_0)}$ at all times. At the critical inflection pressure, the tube makes contact with the braid surface. This is the point where the radius of deformed bladder becomes equal to the radius of the displaced sleeve. Hence,

$$r_o + u_r|_{r_o} = r_b + \hat{u}_r = r_o + \delta + \hat{u}_r \tag{66}$$

and we have

$$r_o + c_1 r_o + \frac{c_2}{r_o} = r_o + \delta + r_b \left\{ \frac{1}{\sin\theta_0} \sqrt{1 - \cos^2\theta_0 \left(1 + \frac{\hat{u}_z}{l_0}\right)^2} - 1 \right\} \tag{67}$$

Simplifying and substituting for $\hat{u}_z$, we get

$$c_1 r_o + \frac{c_2}{r_o} = \delta + r_b \left\{ \frac{1}{\sin\theta_0} \sqrt{1 - \cos^2\theta_0 \left(1 + c_3\right)^2} - 1 \right\} \tag{68}$$

In the above expression, the constants c_1, c_2 and c_3 depend only on applied P_i which is the inflection pressure $\bar{P}_i$. Substituting the values of constants, we get the following equation

$$r_b \left\{ \frac{1}{\sin\theta_0} \times \sqrt{1 - \cos^2\theta_0 \left(1 + \frac{\Lambda_1}{\Lambda_2\left(3\Lambda_1 + 2\Lambda_2\right)} \left[-\frac{\bar{P}_i^2}{r_o^2 - r_i^2} + P_s \frac{\Lambda_1 + \Lambda_2}{\Lambda_1} \right] \right)^2} - 1 \right\} - \frac{r_o}{\Lambda_2\left(3\Lambda_1 + 2\Lambda_2\right)} \left[\frac{2\left(\Lambda_1 + \Lambda_2\right) r_i^2}{\left(r_o^2 - r_i^2\right)} \bar{P}_i - \frac{\Lambda_1}{2} P_s \right] + \delta = 0 \tag{69}$$

where $P_s = \bar{P}_i \dfrac{r_i^2}{r_o^2 - r_i^2} + \dfrac{F}{\pi r_i^2}$. This equation can be numerically solved to find the inflection pressure. For values of applied pressure below $\bar{P}_i$, equation (62) can be used to find the end-point elongation of the MPAM.

3.2.3 Model for second phase-contraction

For values of pressure above $\bar{P}_i$, the contact is established and in this phase, the radial as well as axial displacement of braided sheath will be same as that of the outer surface of silicone tube i.e., $u_r|_{r_o} = \hat{u}_r$ and $u_z|_{l_o} = \hat{u}_z$. Then from the kinematics of braid, equation (64), and from (59) we can write

$$c_1 + \frac{c_2}{r_o^2} = \left(\frac{\sin\theta}{\sin\theta_0} - 1 \right), \quad c_3 = \left(\frac{\cos\theta}{\cos\theta_0} - 1 \right) \tag{70}$$

The above equations represent the constrain on the motion of silicone tube imposed by the braided sleeve.

In this phase, an axial pull on sleeve generates a radial pressure on the outer surface of the silicone tube and vice versa. The total axial end force on the MPAM, F_e, has contributions from three components which are 1) the manually applied axial load F, 2) force acting on the walls due to the applied inner pressure $F_{P_i} = P_i\left(\pi r_i^2\right)$ and 3) any other unaccounted forces such as the static frictional force between the threads and the axial component of force due to the conical shape at the ends which are essential to maintain the static equilibrium of the MPAM. These unaccounted force components are collectively termed F_u. This total axial force F_e is borne unequally by the axial end of silicone tube as well as the nylon braid (ref figure 9).

$$F_e = F + F_{P_i} + F_u = F_{\text{sil}} + F_{\text{nyl}} \tag{71}$$

where F_{sil} represents the axial force acting on silicone tube and F_{nyl} represents the axial force acting on the nylon braid. The force component acting on the braided sleeve is then converted into a radial force based on the kinematics of the braid. The pressure generated by this radial force will constitute the component P_o in the equations (60). Derivation of this radial pressure is detailed in what follows.

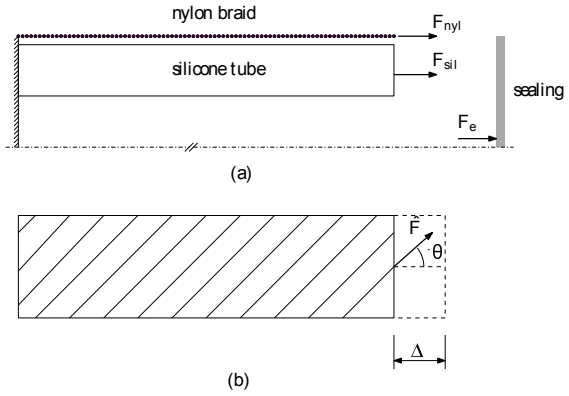

Figure 9: (a) Resolution of axial forces into components acting on braid as well as the silicone tube. (b) Force component acting on a single strand of braid

Since the displacement of the free end of MPAM Δ is same as the deformation of the nylon sleeve Δ_{nyl} as well as the silicone tube Δ_{sil}, it is possible to write the individual components of forces in terms of the end force F_e. We use the material properties of the tube and sheath to calculate the axial displacement of nylon sheath,

$$\Delta_{\text{nyl}} = \frac{\hat{F}b}{\hat{A}_{\text{nyl}}E_{\text{nyl}}}\cos\theta_0 = \frac{F_{\text{nyl}}l_0\cos\theta_0}{m\hat{A}_{\text{nyl}}E_{\text{nyl}}} \tag{72}$$

where $\hat{F} = \dfrac{F_{\text{nyl}}}{m}\cos\theta_0$ is the force acting on a single strand of braid and $\hat{A}_{\text{nyl}}$ is the area of cross section of single nylon strand and E_{nyl} is the modulus of elasticity of nylon (refer Figure 9). Similarly, the axial displacement of silicone tube can be written as

$$\Delta_{\text{sil}} = \frac{F_{\text{sil}}l_0}{A_{\text{sil}}E_{\text{sil}}} \tag{73}$$

where A_{sil} and E_{sil} are the cross section area and Young's modulus of silicone tube. From equations (71), (72) and (73), we get the individual components of forces in terms of end force acting on MPAM as:

$$F_{\text{nyl}} = \frac{F_e m\hat{A}_{\text{nyl}}E_{\text{nyl}}}{m\hat{A}_{\text{nyl}}E_{\text{nyl}} + \cos\theta_0 A_{\text{sil}}E_{\text{sil}}} \tag{74}$$

and

$$F_{\text{sil}} = \frac{F_e\cos\theta_0 A_{\text{sil}}E_{\text{sil}}}{m\hat{A}_{\text{nyl}}E_{\text{nyl}} + \cos\theta_0 A_{\text{sil}}E_{\text{sil}}} \tag{75}$$

The radial force applied by the braid on the outer surface of tube due to the axial pulling force F_{nyl} to maintain static equilibrium of the sheath can be calculated using virtual work principle. From figure 10, we get

$$F_r\delta r + F_{\text{nyl}}\delta l = 0 \tag{76}$$

where δr and δl are the virtual displacements in radial and axial directions, respectively. This quantity can be obtained by taking the variational derivatives of equations (64)

$$\delta l = -b\sin\theta\ \delta\theta, \quad \delta r = b\frac{r_b}{l_0}\frac{\cos\theta}{\tan\theta_0}\delta\theta \tag{77}$$

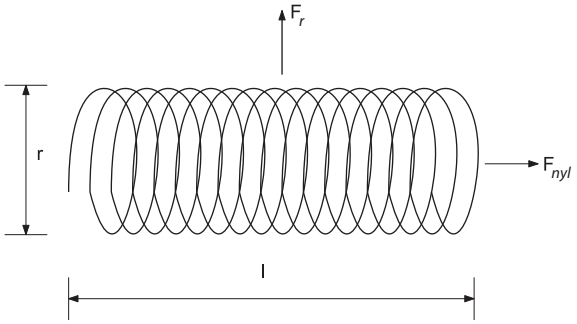

Figure 10: Axial and radial force components acting on the sheath at equilibrium

where $l = l_0 + \hat{u}_z, r = r_b + \hat{u}_r$ are the length and radius of sleeve at angle θ. Substituting in equation (76) and rearranging, we get

$$F_r = F_{\text{nyl}} \frac{l_0}{r_b} \tan\theta \tan\theta_0 \tag{78}$$

The pressure acting on the surface of tube due to this radial force can be calculated by dividing the radial force with the surface area of contact, S_{contact}, between the tube and nylon sheath. The value of S_{contact} is difficult to measure due to the small size of the MPAM. However, we assume that the contact area between the braid and sheath is same as the area of contact between braid in the cross-over points as shown in Figure 11. An analytical expression for the same is given by Davis (mentioned in section 2). Rearranging the expressions (9) and (10), we get

$$S_{\text{contact}} = \left(\frac{\sin^2\theta_{\min} \cos^2\theta_{\min}}{\sin^2\theta \cos^2\theta} \right) S^{\text{cyl}}$$

where S^{cyl} represents the outer surface area of the silicone tube after deforming to the angle θ. The quantity in brackets represents the fraction of total outer surface area of silicone tube where the contact occurs. However, in the either ends of MPAM, the braid stretches, so as to assume the shape of a conical frustum as pointed out in [32] (refer section 2). In this region, the braid densely covers the surface of tube due to the stretching effect (refer Figure 12). Due to this reason, we assume full contact at these ends which are about a length of $\phi = 5$ mm from either ends. Since this end-effect accounts for approximately 25% of the total length of MPAM, this effect needs to be included in the formulation. Then the cylindrical portion of the MPAM will only be $(l_0 - 2\phi)$ mm long. Taking into account the end-effect factor, we can write the total area of contact as:

$$\begin{aligned} S_{\text{contact}} =& \frac{\sin^2\theta_{\min} \cos^2\theta_{\min}}{\sin^2\theta \cos^2\theta} \left[2\pi r \left(l_0 - 2\phi \right) \left(1 + c_3 \right) \right] \\ &+ 2\pi \left(r_b + r \right) \phi \left(1 + c_3 \right) \end{aligned} \tag{79}$$

The pressure P_o acting on the surface of the silicone tube will be due to the braided sleeve, $P_o = P_b = \frac{F_r}{S_{\text{contact}}}$. Substituting the values from equations (74), (78) and (79), we get the braid pressure

$$P_o = \frac{\left[\frac{2\left(F + \pi r_i^2 P_i + F_u\right) m \hat{A}_{\text{nyl}} E_{\text{nyl}}}{2m\hat{A}_{\text{nyl}} E_{\text{nyl}} + 3\cos\theta_0 A_{\text{sil}} E_{\text{sil}}} \right] \frac{l_0}{r_b} \frac{\sin^2\theta}{\cos\theta} \frac{\sin\theta_0}{\cos\theta_0}}{\left[\begin{array}{c} \left\{ \frac{\sin^2\theta_{\min} \cos^2\theta_{\min}}{\sin^2\theta \cos^2\theta} \left[2\pi \left(c_1 r_o + \frac{c_2}{r_o} \right) \left(l_0 - 2\phi \right) \left(1 + c_3 \right) \right] \right\} \\ + 2\pi \left(r_b + c_1 r_o + \frac{c_2}{r_o} \right) \left(\phi + c_3 \phi \right) \end{array} \right]} \tag{80}$$

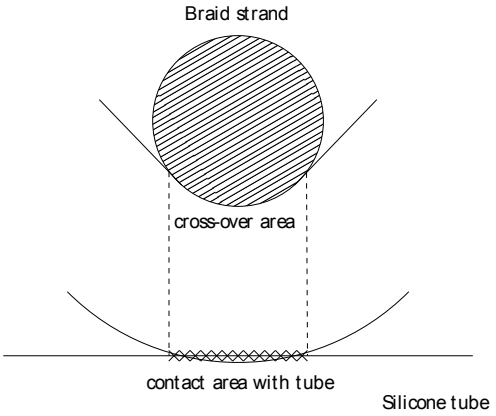

Figure 11: Area of contact between silicone tube and braided sleeve

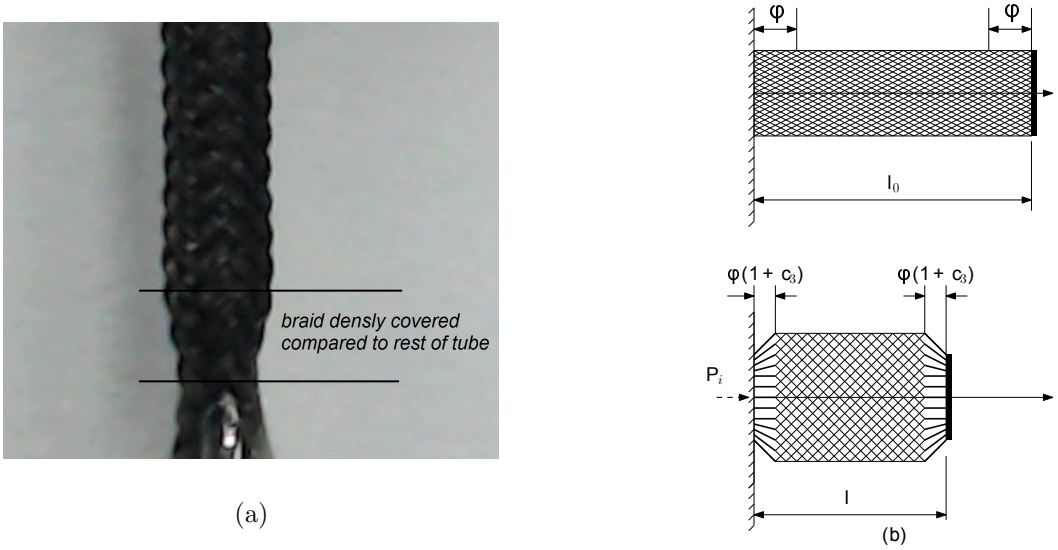

(a)

Figure 12: (a) Conical sections due to the sealing at the ends, (b) Geometrical representation of the conical end-effect during deformation

The six equations in (60) and (70) along with the outer pressure value given by equation (80) can be solved for the six unknown quantities c_1, c_2, c_3, c_4, θ and F_u. Then the final displacements in this contraction phase can be found using the expressions:

$$u_r|_{r=r_o} = c_1 r_o + \frac{c_2}{r_o} \tag{81}$$

$$u_z|_{l=l_o} = c_3 l_o \tag{82}$$

For ease of implementation and to simplify the calculations in second phase, it is possible to consider the second phase as a problem of deformation with the dimensions of tube and sleeve reset to the values at the inflection point [53]

$$r_o \to r_o + \hat{u}|_{r_o} \quad r_i \to r_i + \hat{u}|_{r_i} \quad l_o \to l_o + \hat{u}|_{l_o}$$

where $\bar{(\cdot)}$ denote the corresponding values at the inflection point. For the new arrangement to be in equilibrium, all the traction forces on surfaces must be zero. Hence, we also modify the input pressure to

$P_i \rightarrow P_i - \bar{P}_i$, pressure at the axial end to $P_s \rightarrow P_s - \bar{P}_s$ and the radial outer surface pressure on silicone tube (equal to the pressure applied by braid) to $P_o = P_b \rightarrow P_b - \bar{P}_b$.

3.3 Summary of proposed model

To summarize, the model proposed above constitutes two phases of deformation – an initial elongation phase followed by the contraction phase. In the first phase, the statics of PAM is essentially the statics of the inner tube which is expressed as an inflation problem of a linear thick cylinder. In the second phase, the braided sleeve constraints the tube motion by adding radial pressure on the outer surface of tube. Expression for this radial pressure is formulated based on the kinematics of braid as well as an estimate of the contact surface area between the sleeve and the tube. By applying the derived surface pressure on the tube, the static equations of inner tube is solved along with the kinematic constraint equations, to form the contraction model. One major advantage of using the developed model is that all the axial forces required to maintain the static equilibrium of MPAM – given the values of other applied forces and known components of forces – are collectively termed as F_u and is solved from the six set of equations. Hence finding exact mathematical descriptions of the individual components acting in this direction such as static frictional force, axial force component from the conical ends and other non-linearities are not necessary. If one wishes to study the dependencies of individual axial components of force, one needs to break down F_u into its individual components such as $F_u = F_{\text{static}} + F_{\text{conical}}$ for example. However, it is highly likely that one may overlook many other contributing factors for the axial load resulting in an incomplete formulation. Another advantage of the model is that except the length of the conical section of muscle after deformation which needs to be measured, all other parameters are solved for in our procedure[3].

4 Experimental validation of proposed model

The above derived equations for deformation of MPAM is solved using *fsolve* routine in MATLAB on an desktop PC with 2.0 GHz processor. The routine takes approximately 0.04 seconds to converge with zero initial conditions. Results from the experiments on 40 mm MPAM are plotted against the theoretical values alongside other models for comparison in Figure 13. We can see that the derived model predicts the end-point displacement better than the other compared models with standard error of 4.6% from the maximum deflection. As a comparison, the error values for other models considering the parameters which are obtained from the best curve fit, are 40%, 12%, 7%, 8%, 29%, 8% and 35% for Chou [36], Liu [54], Kothera [43], Andrikopoulos [41], Trivedi [49], Hocking [53] and Sangian [62] models, respectively. The length of conical end section is measured experimentally for this calculation while all the other data are obtained from fabrication. By keeping all the parameters constant, we have plotted results for 60 mm MPAM in Figure 14. As mentioned earlier, except for the Hocking's model (error = 13%), the other models are quite inconsistent in predicting the theoretical contraction with standard error above 20% while the derived model is found to be better, with values predicted within 2% error. In order to check the consistency of winding angle, we plotted the theoretical results for three different winding angles of MPAM and have compared with the experimental values (refer Figure 15). The MPAM wound at higher braid angle was found to have larger gap due to the limitation in winding process. However, the experimental results match the theoretical values with less than 5% error. Theoretical and experimental results for MPAMs of three different lengths wound at 38° initial winding angle are shown in Figure 16. The standard errors between theoretical and experimental values are less than 5%. In order to check the consistency of change in thickness, experiments are conducted on MPAMs fabricated with silicone tube of 1.5 mm outer diameter and 0.5 mm thickness. The results are shown in Figure 17 with error values at a maximum of 6.9%.

In order to find the stiffness of the actuated MPAM, we first pressurized a 45 mm MPAM at 758 kPa pressure where the MPAM contracted by approximately 13 mm. This is kept as the datum for displacement

[3]Youngs modulus of silicone tube used in the paper is obtained from the experimental curve-fit data using Kotheras model (0.345 MPa). This value is also similar for the best fit value of the linear term in Hockings model (0.352 MPa)

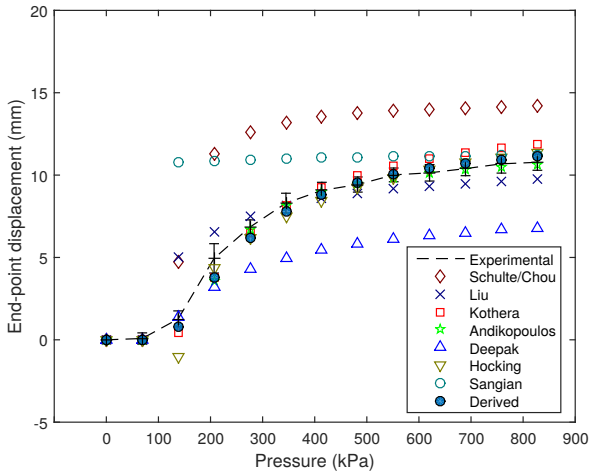

Figure 13: End-point displacement vs applied pressure for 40 mm MPAM. $\theta_0 = 36°$, $r_i = 0.25$ mm, $r_o = 0.55$ mm, $r_n = 0.04$ mm, $m = 30$, $\phi = 5$mm, $E = 0.35$ MPa, $\nu = 0.499$, $F = 0.05$ N.

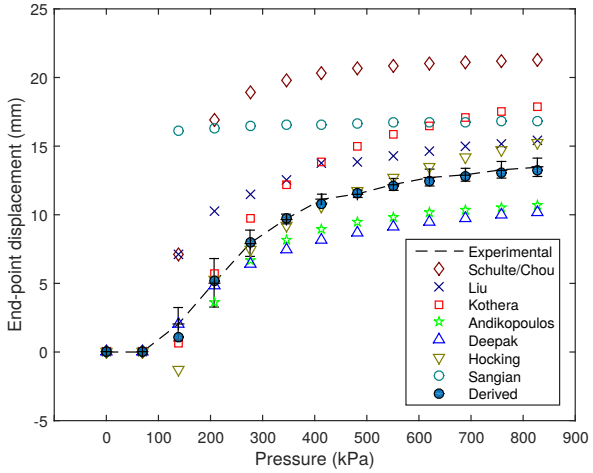

Figure 14: End-point displacement vs applied pressure for 60 mm MPAM. $\theta_0 = 36°$, $r_i = 0.25$ mm, $r_o = 0.55$ mm, $r_n = 0.04$ mm, $m = 30$, $\phi = 5$mm, $E = 0.35$ MPa, $\nu = 0.499$, $F = 0.05$ N.

measurements. Then axial loads are applied in terms of known weights added at the free end of MPAM and the corresponding displacements are measured from the datum. By plotting applied axial force against displacement and calculating the slope, the stiffness value is found to be 0.94 N/mm (ref Figure 18)[4]. This value over-predicts the actual stiffness of 0.63 N/mm by 49%. Except Andrikopoulos' model[5] which gives 0.92 N/mm and Liu's model which gives 1.96 N/m stiffness, other models show very large error in the stiffness value (in the order of 10) and are not plotted hence. We found from observation that at higher loads, the effect of conical ends are prominent, since the MPAM is axially stretched due to this loads. Due to this stretching caused by applied loads, the value ϕ is higher. We have not developed an analytical model for

[4]It may be noted that the total end-point displacement in this case will be the sum of end-point displacement during free contraction and the displacement due to the applied load.

[5]Since $k_f^{(2)}$ in Andrikopoulos' model is evaluated using experimental data, better prediction of stiffness is expected.

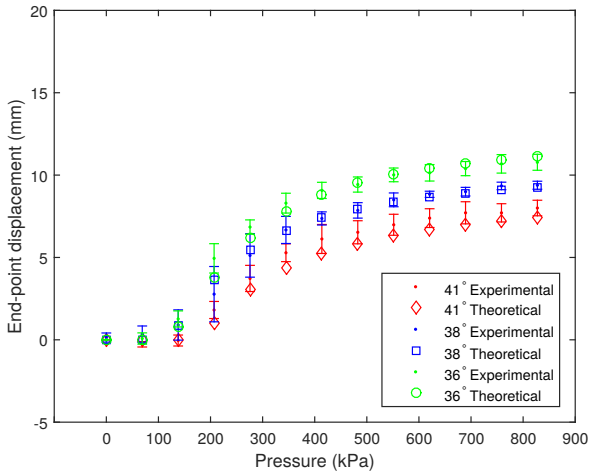

Figure 15: End-point displacement vs applied pressure for different angle of windings. $l_o = 40$ mm, $r_i = 0.25$ mm, $r_o = 0.55$ mm, $r_n = 0.04$ mm, $m = 30$, $\phi = 5$mm, $E = 0.35$ MPa, $\nu = 0.499$, $F = 0.05$ N.

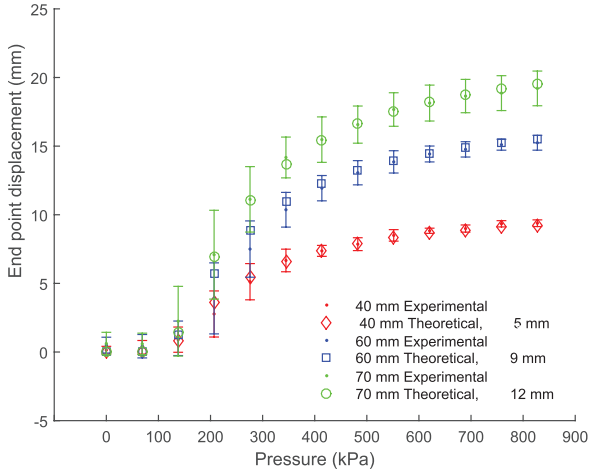

Figure 16: End-point displacement vs applied pressure for MPAM wound at 38° angle. $r_i = 0.25$ mm, $r_o = 0.55$ mm, $r_n = 0.04$ mm, $m = 30$, $E = 0.35$ MPa, $\nu = 0.499$, $\phi = \{5, 9, 12\}$ mm, $F = 0.05$ N.

calculating the value of ϕ, but a proportional increase of the value ϕ based on the applied force, say $\hat{\phi} = \phi \frac{F}{k}$ (where k is a scaling factor), is shown to give much better approximation at higher loads. The proportional factor can be determined by minimizing the error between actual and theoretical values for a single data point in the pressure-deformation plot. This corrected model is also plotted in Figure 18.

The final theoretical braid angle for an extrapolated pressure value is plotted in the Figure 19. We can see that the braid angle asymptotically reaches the locking limit of 54.7°. In this case, the limit is slightly overshot at higher pressures. This is because we have not considered the scaling factor $S^{(1)}_{\text{scale}}$ for contact area mentioned in the Cadwell's derivation, which, is in fact a correction factor for the underestimation of radial force on tube. However, since we do not have definitive calculations to determine S_{scale} except by empirical

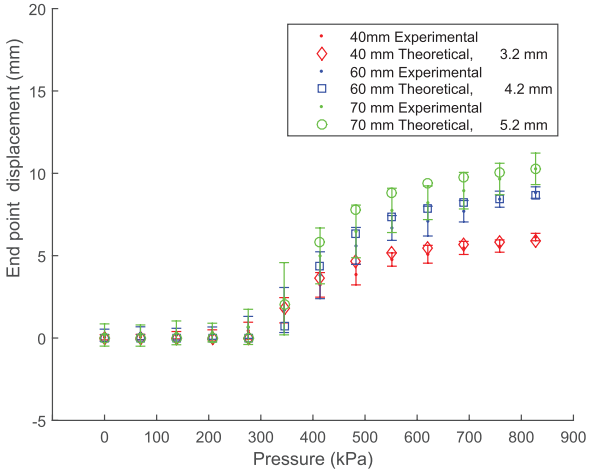

Figure 17: End-point displacement vs applied pressure for MPAM with tube O.D 1.5 mm. $\theta_0 = 35°$, $r_i = 0.25$ mm, $r_n = 0.04$ mm, $m = 30$, $E = 0.35$ MPa, $\nu = 0.499$, $\phi = \{3.2, 4.2, 5.2\}$ mm, $F = 0.05$ N.

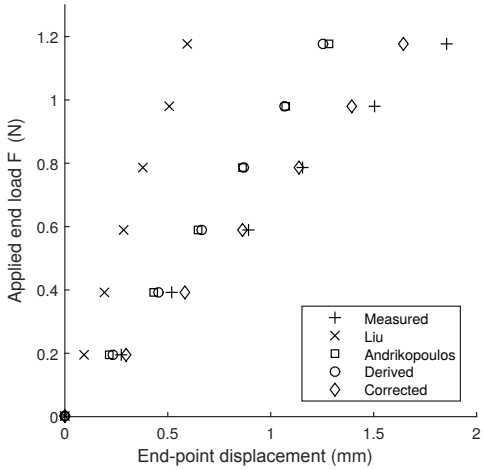

Figure 18: Axial force vs displacement from fully contracted state. $P_i = 758$ kPa, $\alpha = 36°$, $l_o = 45$ mm, $r_i = 0.25$ mm, $r_o = 0.55$ mm, $r_n = 0.04$ mm, $m = 30$, $\phi = 5$mm, $E = 0.35$ MPa, $\nu = 0.499$

measures, we are not further considering the same.

From the above validation experiments we can conclude that, the developed model is able to predict the deformation of MPAM with good accuracy and consistency compared to other models. Theoretical model is able to predict the actual deformation with less than 7% error. The consistency of the model with respect to change in parameters such as initial length, initial braiding angle as well as the thickness of inner tube is experimentally validated. The developed model shows large error in predicting the stiffness of MPAM. However, an increase in the length of conical section proportional to the applied force shows much better conformation with the experimental value of stiffness. The application of this model on PAMs of diameter larger than 5 mm is not verified by our validation experiments and hence it is not possible to claim the accuracy of this modeling strategy on regular sized PAMs.

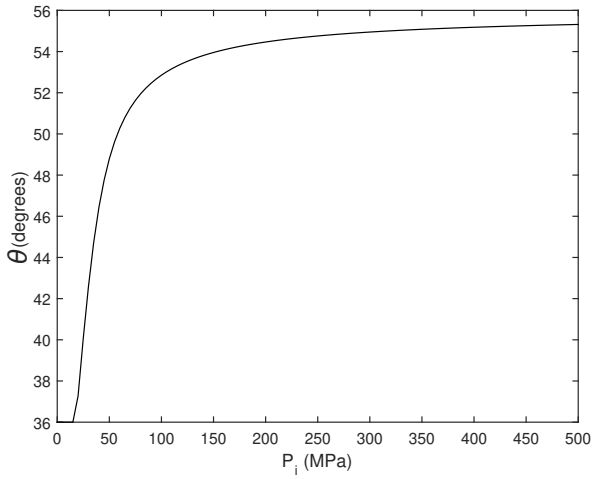

Figure 19: Evolution of final braid angle for large pressure range

5 Conclusions

Tondu's review paper [32] concludes with an open question of whether it is possible to achieve an accurate mathematical description of the physics behind the actuation of Pneumatic Artificial Muscles (PAMs). Till date, many researchers have attempted to answer this question, which resulted in a variety of modeling techniques some of which, even though are not exact representation of the physical phenomena, seem to suit the purpose of application in PAM enabled robots and mechanisms. A detailed survey of various modeling considerations for PAM in this regard have been carried out in this paper and this is the first contributions of this work. From the first model mentioned in Gaylord's patent for fluidic muscle actuators, many improvements have been made so far by adding correction factors, considering better modeling assumptions and including factors arising from other physical aspects of the PAM which are detailed in this paper. As shown in [81], where the authors picked static force component from [22] and the frictional forces from [37] for their model, it may be possible for researchers to combine only relevant component of forces as per the application. Since understanding the hysteresis of PAM in a phenomenological point of view is still a challenge, many applications rely heavily on empirical formulations. In this regard, a few empirical formulations are also discussed so that the reader can selectively apply the models convenient to their application.

Secondly, it was found that most of the phenomenological models for PAM seem to be inconsistent with the statics of miniaturized PAMs especially to the change in initial parameters. A novel modeling strategy different from the conventional energy balance concept and which considers two major physical aspects of MPAM – the material property of the Silicone tube and the non cylindrical end-effects – has been derived. As opposed to the conventional modeling strategy, the complex axial components of force such as friction as well as the component of radial force from conical ends required to maintain static equilibrium of the MPAM are obtained by solving the model. Hence, separate accurate formulation of these terms are not necessary. The derived model could accurately predict the deformation of MPAM for a given applied pressure with less than 7% error. The consistency of model with changes in initial parameters such as length, braid angle as well as the thickness of tube is verified by validation experiments. The standard error between experimental results and theoretical results for different initial parameters is much less compared to the other models available in the literature. While the model under predicts the stiffness of pressurized MPAM, this is identified as due to the limitation in the model in addressing the stretching of conical end-section due to the applied force. A correction applied to the end-section length proportional to the applied force showed better conformation with the experimental results. The model also predicts the theoretical limiting angle of 54.7° at extrapolated pressure values.

Due to the incomparable advantages of PAMs, many interesting developments are being made in this field of research. For example, in [82], a new design of PAM with integrated sensing mechanism is introduced where one of the braid fiber is replaced with conducting wire so that by measuring the electrical resistance, the contraction characteristics can be directly measured. A similar method is shown in [83] where the electrical inductance is measured instead of the wire resistance. Even though both works are intended to measure the contraction of PAM, it may be possible to use the same techniques to directly measure the complex force interactions from the PAM for validating the mathematical models. By using an 'agonistic-antagonistic' pair of muscles, it is shown in [65] and [30] that hysteresis effect can be tackled in the actual implementation of PAM. While PAM is primarily viewed as a linear actuator, in [84] and [85] the authors have discussed fabrication techniques for pneumatic bending actuators which can produce forces as well as moments in the tip. Many researchers have also come up with methods other than the pneumatic pressure for actuating the muscle [58], [81] and [86]. In such cases, while most of the forces acting on the actuator remain the same, new components are added in the statics model, such as in the case of [86], where a thermally activated paraffin is used instead of compressed air. Similarly, we also find a study of knitted PAMs [87] and flat PAMs [88] in the recent literature. With such enormous emphasis and rapid improvement in this field of actuation, we hope that this paper will be useful for upcoming and continuing researchers and engineers.

Acknowledgement

The authors would like to thank M/s. Electrical and Allied Products, Bangalore, India, for providing the braiding facilities. This work was partly funded by a grant from Robert Bosch Centre for Cyber Physical Systems.

References

[1] R. H. Gaylord (1958), "Fluid actuated motor system and stroking device", *US Patent 2,844,126* (July 22 1958).

[2] L. Joseph (1960), "Artificial muscle", *Life* **14**, pp. 87–88.

[3] T. E. Pillsbury, C. S. Kothera, N. M. Wereley (2015), " Effect of bladder wall thickness on miniature pneumatic artificial muscle performance", *Bioinspiration & Biomimetics*, **10** (5), pp. 055006.

[4] Festo Fluidic Muscle, Festo Didactic Inc., 607 Industrial Way West, Eatontown NJ 07724, Available: www.festo.com, Date accessed 12/04/2018.

[5] J. E. Takosoglu, P. A. Laski, S. Blasiak, G. Bracha, D. Pietrala (2016), "Determining the static characteristics of pneumatic muscles", *Measurement and Control*, **49** (2), pp. 62–71.

[6] A. De Greef, P. Lambert, A. Delchambre (2009), "Towards flexible medical instruments: Review of flexible fluidic actuators", *Precision Engineering*, **33** (4), pp. 311–321.

[7] S. D. Prior, P. R. Warner, A. S. White, J. Parsons, R. Gill (1993), "Actuators for rehabilitation robots", *Mechatronics*, **3** (3), pp. 285–294.

[8] T. Takagi, Y. Sakaguchi (1986), "Pneumatic actuator for manipulator", *US Patent 4,615,260* (October 7 1986).

[9] A. Moers, M. De Volder, D. Reynaerts (2012), "Integrated high pressure microhydraulic actuation and control for surgical instruments", *Biomedical Microdevices*, **14** (4), pp. 699–708.

[10] K. Ashwin, D. P. Jose, A. Ghosal (2015), "Modeling and analysis of a flexible end-effector for actuating endoscopic catheters", *Proceedings of the 14th IFToMM World Congress 2015*, pp. 113–120.

[11] H. M. Le, T. N. Do, S. J. Phee (2016), "A survey on actuators-driven surgical robots", *Sensors and Actuators A: Physical*, **247**, pp. 323–354.

[12] T. Noritsugu, T. Tanaka (1997), "Application of rubber artificial muscle manipulator as a rehabilitation robot", *IEEE/ASME Transactions on Mechatronics*, **2** (4), pp. 259–267.

[13] P. K. Jamwal, S. Q. Xie, S. Hussain, J. G. Parsons (2014), "An adaptive wearable parallel robot for the treatment of ankle injuries", *IEEE/ASME Transactions on Mechatronics*, **19** (1), pp. 64–75.

[14] G. Andrikopoulos, G. Nikolakopoulos, S. Manesis (2011), "A survey on applications of pneumatic artificial muscles", *19th IEEE Mediterranean Conference on Control & Automation (MED) 2011*, pp. 1439–1446.

[15] H. Li, K. Kawashima, K. Tadano, S. Ganguly, S. Nakano (2013), "Achieving haptic perception in forceps manipulator using pneumatic artificial muscle", *IEEE/ASME Transactions on Mechatronics*, **18** (1), pp. 74–85.

[16] I. Doric, A. Reitberger, S. Wittmann, R. Harrison, T. Brandmeier (2014), "1 A novel approach for the test of active pedestrian safety systems", *IEEE Transactions on Intelligent Transportation Systems*, **18** (5), pp. 1299–1312.

[17] A. P. Tjahyono, K. C. Aw, H. Devaraj, W. Surendra, E. Haemmerle, J. Travas-Sejdic (2013), "A five-fingered hand exoskeleton driven by pneumatic artificial muscles with novel polypyrrole sensors", *Industrial Robot: An International Journal*, **40** (3), pp. 251–260.

[18] S. C. Obiajulu, E. T. Roche, F. A. Pigula, C. J. Walsh (2013), "Soft pneumatic artificial muscles with low threshold pressures for a cardiac compression device", *ASME 2013 International Design Engineering Technical Conferences and Computers and Information in Engineering Conference*, pp. V06AT07A009–V06AT07A009.

[19] M. De Volder, A. Moers, D. Reynaerts (2011), "Fabrication and control of miniature Mckibben actuators", *Sensors and Actuators A: Physical*, **166** (1), pp. 111–116.

[20] S. Chakravarthy, K. Aditya, A. Ghosal (2014), "Experimental characterization and control of miniaturized pneumatic artificial muscle", *Journal of Medical Devices*, **8** (4), pp. 041011-041019.

[21] M. Bryant, M. A. Meller, E. Garcia (2013), "Toward variable recruitment fluidic artificial muscles", *ASME 2013 Conference on Smart Materials, Adaptive Structures and Intelligent Systems*, pp. V002T06A014–V002T06A014.

[22] M. Bryant, M. A. Meller, E. Garcia (2014), "Variable recruitment fluidic artificial muscles: modeling and experiments", *Smart Materials and Structures*, **23** (7), pp. 074009.

[23] M. A. Meller, J. B. Chipka, M. J. Bryant, E. Garcia (2015), "Modeling of the energy savings of variable recruitment mckibben muscle bundles" *Bioinspiration, Biomimetics, and Bioreplication, Proceedings of SPIE - The International Society for Optical Engineering Vol 9429*, pp. 94290S.

[24] R. M. Robinson, C. S. Kothera, N. M. Wereley (2015), "Variable recruitment testing of pneumatic artificial muscles for robotic manipulators", *IEEE/ASME Transactions on Mechatronics*, **20** (4), pp. 1642–1652.

[25] M. Meller, J. Chipka, A. Volkov, M. Bryant, E. Garcia (2016), "Improving actuation efficiency through variable recruitment hydraulic Mckibben muscles: modeling, orderly recruitment control, and experiments" *Bioinspiration & Biomimetics*, **11** (6), pp. 065004.

[26] S. Kurumaya, H. Nabae, G. Endo, K. Suzumori (2017), "Design of thin Mckibben muscle and multifilament structure", *Sensors and Actuators A: Physical*, **261**, pp. 66–74.

[27] B. Wang, K. C. Aw, M. Biglari-Abhari, A. McDaid (2016), "Design and fabrication of a fiber-reinforced pneumatic bending actuator", *2016 IEEE International Conference on Advanced Intelligent Mechatronics (AIM)*, pp. 83–88.

[28] W. McMahan, V. Chitrakaran, M. Csencsits, D. Dawson, I. D. Walker, B. A. Jones, M. Pritts, D. Dienno, M. Grissom, C. D. Rahn (2006), "Field trials and testing of the octarm continuum manipulator", *Proceedings of IEEE International Conference on Robotics and Automation (ICRA 2006)*, pp. 2336–2341.

[29] J. Bishop-Moser, G. Krishnan, S. Kota (2013), "Force and moment generation of fiber-reinforced pneumatic soft actuators", *Proceedings of IEEE/RSJ International Conference on Intelligent Robots and Systems (IROS 2013)*, pp. 4460–4465.

[30] R. M. Robinson, C. S. Kothera, N. M. Wereley (2015), "Quasi-static nonlinear response of pneumatic artificial muscles for both agonistic and antagonistic actuation modes", *Journal of Intelligent Material Systems and Structures*, **26** (7), pp. 796–809.

[31] R. M. Robinson, C. S. Kothera, R. M. Sanner, N. M. Wereley (2016), " Nonlinear control of robotic manipulators driven by pneumatic artificial muscles", *IEEE/ASME Transactions on Mechatronics*, **21** (1), pp. 55–68.

[32] B. Tondu (2012), "Modelling of the Mckibben artificial muscle: A review", *Journal of Intelligent Material Systems and Structures*, **23** (3), pp. 225–253.

[33] H. Schulte (1961), "The application of external power in prosthetics and orthotics, The Characteristics of the McKibben Artificial Muscle", *National Research Council*, pp. 874.

[34] G. K. H. S. L. Das, B. Tondu, F. Forget, J. Manhes, O. Stasse, P. Souères (2016), "Controlling a multi-joint arm actuated by pneumatic muscles with quasi-ddp optimal control", *in: Proceedings of IEEE/RSJ International Conference on Intelligent Robots and Systems (IROS 2016)*, pp. 521–528.

[35] T. E. Pillsbury, N. M. Wereley, Q. Guan (2017), "Comparison of contractile and extensile pneumatic artificial muscles", *Smart Materials and Structures*, **26** (9), pp. 095034.

[36] C. P. Chou, B. Hannaford (1996), "Measurement and modeling of Mckibben pneumatic artificial muscles", *IEEE Transactions on Robotics and Automation*, **12** (1), pp. 90–102.

[37] B. Tondu, P. Lopez (2000), "Modeling and control of Mckibben artificial muscle robot actuators", *IEEE Control Systems*, **20** (2), pp. 15–38.

[38] T. Itto, K. Kogiso (2011), "Hybrid modeling of Mckibben pneumatic artificial muscle systems", *in: IEEE International Conference on Industrial Technology (ICIT 2011)*, pp. 65–70.

[39] S. Davis, D. G. Caldwell (2006), "Braid effects on contractile range and friction modeling in pneumatic muscle actuators", *The International Journal of Robotics Research*, **25** (4), pp. 359–369.

[40] E. Chapman, M. Macleod, M. Bryant (2015), "Electrohydraulic modeling of a fluidic artificial muscle actuation system for robot locomotion", *2015 ASME Conference on Smart Materials, Adaptive Structures and Intelligent Systems*, pp. V001T03A005–V001T03A005.

[41] G. Andrikopoulos, G. Nikolakopoulos, S. Manesis (2016), "Novel considerations on static force modeling of pneumatic muscle actuators", *IEEE/ASME transactions on Mechatronics*, **21** (6), pp. 2647–2659.

[42] W. F. Carlo Ferraresi, W. Walter Franco, A. Bertetto (2001), "Flexible pneumatic actuators: a comparison between the mckibben and the straight fibres muscles", *Journal of Robotics and Mechatronics*, **13**, pp. 56–63.

[43] C. S. Kothera, M. Jangid, J. Sirohi, N. M. Wereley (2009), "Experimental characterization and static modeling of Mckibben actuators", *Journal of Mechanical Design*, **131** (9), pp. 091010.

[44] N. Delson, T. Hanak, K. Loewke, D. N. Miller (2005), "Modeling and implementation of Mckibben actuators for a hopping robot", *Proceedings of 12th International Conference on Advanced Robotics (ICAR 2005)*, pp. 833–840.

[45] M. Mooney (1940), "A theory of large elastic deformation", *Journal of Applied Physics*, **11** (9) pp. 582–592.

[46] R. Rivlin (1948), "Large elastic deformations of isotropic materials. IV. Further developments of the general theory", *Phil. Transactions of Royal Society of London A*, **241** pp. 379–397.

[47] G. K. Klute, B. Hannaford (2000), "Accounting for elastic energy storage in Mckibben artificial muscle actuators", *Journal of Dynamic Systems, Measurement, and Control*, **122** (2), pp. 386–388.

[48] B. K. Woods, C. S. Kothera, N. M. Wereley (2011), "Wind tunnel testing of a helicopter rotor trailing edge flap actuated via pneumatic artificial muscles", *Journal of Intelligent Material Systems and Structures*, **22** (13), pp. 1513–1528.

[49] D. Trivedi, A. Lotfi, C. D. Rahn (2008), "Geometrically exact models for soft robotic manipulators", *IEEE Transactions on Robotics*, **24** (4), pp. 773–780.

[50] B. Kim, S. B. Lee, J. Lee, S. Cho, H. Park, S. Yeom, S. H. Park, "A comparison among Neo-Hookean model, Mooney-Rivlin Model and Ogden model for cholorprene rubber", *International Journal of Precision Engineering and Manufacturing*, **13** (5), pp. 759–764.

[51] G. Wang, N. M. Wereley, T. Pillsbury (2015), "Non-linear quasi-static model of pneumatic artificial muscle actuators", *Journal of Intelligent Material Systems and Structures*, **26** (5), pp. 541–553.

[52] M. D. Doumit (2009), "Characterization, modeling and design of the braided pneumatic muscle", *Ph.D. Thesis, University of Ottawa (Canada).*

[53] E. G. Hocking, N. M. Wereley (2012), "Analysis of nonlinear elastic behavior in miniature pneumatic artificial muscles", *Smart Materials and Structures*, **22** (1), pp. 014016.

[54] W. Liu, C. Rahn (2003), "Fiber-reinforced membrane models of Mckibben actuators", *Transactions of the ASME Journal of Applied Mechanics*, **70** (6), pp. 853–859.

[55] A. Kydoniefs, E. P. Salathe (1974), "Finite cylindrical deformations of a reinforced elastic tube", *International Journal of Engineering Science*, **12** (6), pp. 519–535.

[56] A. E. Green, J. E. Adkins (1970), "Large elastic deformations", *Clarendon Press, Vol. 1,*.

[57] E. Ball, E. Garcia (2016), "Effects of bladder geometry in pneumatic artificial muscles", *Journal of Medical Devices,*, **10** (4), pp. 041001

[58] N. Goulbourne (2009), " A mathematical model for cylindrical, fiber reinforced electro-pneumatic actuators", *International Journal of Solids and Structures*, **46** (5), pp. 1043–1052.

[59] D. Chen, K. Ushijima (2014), "Prediction of the mechanical performance of Mckibben artificial muscle actuator", *International Journal of Mechanical Sciences*, **78**, pp. 183–192.

[60] W. Zhang, M. L. Accorsi, J. W. Leonard (2005), "Analysis of geometrically nonlinear anisotropic membranes: application to pneumatic muscle actuators", *Finite Elements in Analysis and Design*, **41** (9-10), pp. 944–962.

[61] M. G. Antonelli, P. Beomonte Zobel, F. Durante, T. Raparelli (2017), "Numerical modelling and experimental validation of a mckibben pneumatic muscle actuator", *Journal of Intelligent Material Systems and Structures*, **28** (19), pp. 2737–2748.

[62] D. Sangian, S. Naficy, G. M. Spinks, B. Tondu (2015), "The effect of geometry and material properties on the performance of a small hydraulic Mckibben muscle system", *Sensors and Actuators A: Physical*, **234**, pp. 150–157

[63] A. Pujana-Arrese, A. Mendizabal, J. Arenas, R. Prestamero, J. Landaluze (2010), "Modelling in modelica and position control of a 1-dof set-up powered by pneumatic muscles", *Mechatronics*, **20** (5), pp. 535–552.

[64] S. Ganguly, A. Garg, A. Pasricha, S. Dwivedy (2012), "Control of pneumatic artificial muscle system through experimental modelling", *Mechatronics*, **22** (8), pp. 1135–1147.

[65] L. Sui, S. Xie (2013), "Modelling of pneumatic muscle actuator and antagonistic joint using linearised parameters", *International Journal of Biomechatronics and Biomedical Robotics* , **2** (2-4), pp. 67–74.

[66] B. Tondu (2012), "Closed-loop position control of artificial muscles with a single integral action: Application to robust positioning of mckibben artificial muscle", *2013 IEEE International Conference on Mechatronics (ICM)*, pp. 718–723.

[67] B. Tondu (2015), "Single linear integral action control for closed-loop positioning of a biomimetic actuator with artificial muscles", *2015 European Control Conference (ECC)*, pp. 3585–3590.

[68] M. Van Damme, P. Beyl, B. Vanderborght, R. Van Ham, I. Vanderniepen, R. Versluys, F. Daerden, D. Lefeber (2008), "Modeling hysteresis in pleated pneumatic artificial muscles", *2008 IEEE Conference on Robotics, Automation and Mechatronics*, pp. 471–476.

[69] J. A. Stakvik, M. R. P. Ragazzon, A. A. Eielsen, J. T. Gravdahl, (2015), "On implementation of the Preisach model: identification and inversion for hysteresis compensation", *Modeling, Identification and Control*, **36** (3), pp. 133–142.

[70] W. D. Iwan (1966), "A distributed-element model for hysteresis and its steady-state dynamic response", *Journal of Applied Mechanics*, **33** (4), pp. 893–900.

[71] T. V. Minh, T. Tjahjowidodo, H. Ramon, H. Van Brussel (2009), "Control of a pneumatic artificial muscle (PAM) with model-based hysteresis compensation" *IEEE/ASME International Conference on Advanced Intelligent Mechatronics (AIM 2009)*, pp. 1082–1087.

[72] T. Vo-Minh, T. Tjahjowidodo, H. Ramon, H. Van Brussel (2011), "A new approach to modeling hysteresis in a pneumatic artificial muscle using the maxwell-slip model", *IEEE/ASME Transactions on Mechatronics*, **16** (1), pp. 177–186.

[73] C. J. Lin, C. R. Lin, S. K. Yu, C. T. Chen (2015), "Hysteresis modeling and tracking control for a dual pneumatic artificial muscle system using Prandtl–Ishlinskii model", *Mechatronics*, **28**, pp. 35–45.

[74] M. Ismail, F. Ikhouane, J. Rodellar (2009), "The hysteresis Bouc-Wen model, a survey", *Archives of Computational Methods in Engineering* , **16** (2), pp. 161–188.

[75] A. Visintin (2013), "Differential Models of Hysteresis Vol. III", *Springer Science & Business Media*.

[76] S. Xie, J. Mei, H. Liu, Y. Wang (2018), "Hysteresis modeling and trajectory tracking control of the pneumatic muscle actuator using modified Prandtl–Ishlinskii model", *Mechanism and Machine Theory*, **120**, pp. 213–224.

[77] H. Aschemann, D. Schindele (2014), "Comparison of model-based approaches to the compensation of hysteresis in the force characteristic of pneumatic muscles", *IEEE Transactions on Industrial Electronics* , **61** (7), pp. 3620–3629.

[78] Y. Liu, X. Zang, Z. Lin, X. Liu, J. Zhao (2017), "Modelling length/pressure hysteresis of a pneumatic artificial muscle using a modified Prandtl-Ishlinskii model", *Strojniški vestnik-Journal of Mechanical Engineering*, **63** (1), pp. 56–64.

[79] L. Hao, H. Yang, Z. Sun, C. Xiang, B. Xue (2017), "Modeling and compensation control of asymmetric hysteresis in a pneumatic artificial muscle", *Journal of Intelligent Material Systems and Structures*, **28** (19), pp. 2769–2780.

[80] C. S. Jog (2015), "Continuum mechanics, Vol. 1", *Cambridge University Press*.

[81] E. Chapman, T. Jenkins, M. Bryant (2016), "Parametric study of a fluidic artificial muscle actuated electrohydraulic system", *2016 ASME Conference on Smart Materials, Adaptive Structures and Intelligent Systems*, pp. V002T06A003–V002T06A003.

[82] S. Wakimoto, J. Misumi, K. Suzumori (2016), "New concept and fundamental experiments of a smart pneumatic artificial muscle with a conductive fiber", *Sensors and Actuators A: Physical*, **250**, pp. 48–54.

[83] O. Erin, N. Pol, L. Valle, Y. L. Park (2016), " Design of a bio-inspired pneumatic artificial muscle with self-contained sensing", *2016 IEEE 38th Annual International Conference of the Engineering in Medicine and Biology Society (EMBC)*, pp. 2115–2119.

[84] H. Al-Fahaam, S. Davis, S. Nefti-Meziani (2018), "The design and mathematical modelling of novel extensor bending pneumatic artificial muscles (EBPAMS) for soft exoskeletons", *Robotics and Autonomous Systems*, **99**, pp. 63–74.

[85] J. Bishop-Moser, S. Kota (2015), "Design and modeling of generalized fiber-reinforced pneumatic soft actuators", *IEEE Transactions on Robotics*, **31** (3), pp. 536–545.

[86] D. Sangian, S. Naficy, G. M. Spinks (2016), "Thermally activated paraffin-filled Mckibben muscles", *Journal of Intelligent Material Systems and Structures*, **27** (18), pp. 2508–2516.

[87] E. J. Ball, M. A. Meller, J. B. Chipka, E. Garcia (2016), "Modeling and testing of a knitted-sleeve fluidic artificial muscle", *Smart Materials and Structures*, **25** (11), pp. 115024.

[88] Y. L. Park, J. Santos, K. G. Galloway, E. C. Goldfield, R. J. Wood (2014), "A soft wearable robotic device for active knee motions using flat pneumatic artificial muscles", *IEEE International Conference on Robotics and Automation (ICRA 2014)*, pp. 4805–4810.